TAMPEREEN TEKNILLINEN YLIOPISTO
TAMPERE UNIVERSITY OF TECHNOLOGY

JUHO PÖLÖNEN

MRI SHAPE ANALYSIS OF MIDBRAIN IN PARKINSON'S DISEASE

Master of Science thesis

Examiners: Prof. Hannu Eskola,
D.Sc. (Tech) Kirsi Holli-Helenius
Examiner and topic approved by the Faculty Council of the Faculty of Computing and Electrical Engineering on September 9th 2015

ABSTRACT

JUHO PÖLÖNEN: MRI shape analysis of midbrain in Parkinson's disease
Tampere University of technology
Master of Science Thesis, 48 pages, 2 Appendix pages
April 2016
Master's Degree Programme in Electrical engineering
Major: Biomeasurements and imaging
Examiners: Professor Hannu Eskola, D.Sc. (Tech) Kirsi Holli-Helenius

Keywords: image analysis, MRI, Parkinson's disease

Magnetic resonance imaging (MRI) is an imaging modality that uses magnetic fields, field gradients and radio waves to form images of different tissues within the body. It is often the best choice for structural brain imaging due to high soft tissue contrast. The current role of medical imaging in the diagnosis of Parkinson's disease (PD) is insignificant. However, several studies of quantitative image analysis methods have shown promising results in the detection of the structural changes related to PD.

In this Master's thesis, quantitative shape analysis was used to study the structural differences of the substantia nigra pars reticulata (SNr) and the red nucleus (RN) between PD patients and healthy controls. The material consisted of T2 -weighted 3 T MR images of 29 patients and 20 controls. The images were segmented using manual thresholding, k-means clustering and region growing. After the segmentation, 13 shape factors were calculated for the brain structures in both hemispheres and the results were analyzed statistically using the Mann-Whitney U test.

Out of the three segmentation methods, only the k-means clustering provided images that showed statistically significant differences between the patients and the healthy controls. However, the differences could only be observed in the left hemisphere. The shape factors calculated from these images showed that the overall sizes of the RN and the SNR were greater in the patient group. They also indicated increased irregularity among the PD patients. These findings correlate with current pathophysiological and anatomical knowledge of PD.

TIIVISTELMÄ

JUHO PÖLÖNEN: MRI shape analysis of midbrain in Parkinson's disease
Tampereen teknillinen yliopisto
Diplomityö, 48 sivua, 2 liitesivua
Huhtikuu 2016
Sähkötekniikan diplomi-insinöörin tutkinto-ohjelma
Pääaine: Biomittaukset ja kuvantaminen
Tarkastajat: Professori Hannu Eskola, TkT Kirsi Holli-Helenius

Avainsanat: kuva-analyysi, magneettikuvaus, Parkinsonin tauti

Magneettikuvaus on kuvantamismenetelmä, joka hyödyntää magneettikenttiä, kenttägradientteja ja radioaaltoja kontrastin muodostamisessa eri kudosten välille. Korkean pehmytkudoskontrastin ansiosta magneettikuvaus on yksi parhaista menetelmistä aivojen rakenteelliseen kuvantamiseen. Nykyisistä kuvantamismenetelmistä ei ole juuri apua Parkinsonin taudin diagnoosissa. Monet kvantitatiiviseen kuva-analyysiin liittyvät tutkimukset ovat kuitenkin tuottaneet lupaavia tuloksia Parkinsonin tautiin liittyvien aivojen rakenteellisten muutosten havaitsemisessa.

Tässä diplomityössä käytettiin kvantitatiivista muotoanalyysia mustatumakkeen pars reticulatan ja punatumakkeen rakenteellisten erojen tutkimiseen Parkinson -potilaiden ja verrokkiryhmän välillä. Materiaali koostui 29 Parkinson -potilaan ja 20 verrokin T2 -painotteisista 3 T -magneettikuvista. Kuvat segmentoitiin käyttämällä kynnysarvomenetelmää, k-means klusterointia ja alueen kasvatusta. Segmentoinnin jälkeen kuvista laskettiin 13 muotoparametria tutkituille aivorakenteille molemmissa aivopuoliskoissa ja tulokset analysoitiin tilastollisesti käyttäen Mann-Whitney U -testiä.

Ainoastaan k-means klusteroinnilla segmentoiduista kuvista lasketut muotoparametrit tuottivat tilastollisesti merkittäviä eroja potilaiden ja verrokkien välille. Erot olivat kuitenkin havaittavissa vain vasemmassa aivopuoliskossa. Kyseiset muotoparametrit osoittivat, että molempien aivorakenteiden koko oli suurempi potilailla kuin verrokeilla. Aivorakenteiden muodot oli myös epäsäännöllisempiä potilasryhmässä. Nämä havainnot korreloivat Parkinsonin taudin patofysiologisen ja anatomisen tietämyksen kanssa.

PREFACE

This Master's thesis was done at the Medical Imaging Centre of Tampere University Hospital and at the Department of Electronics and Communications Engineering of Tampere University of Technology.

I would like to thank my examiners, Professor Hannu Eskola and D.Sc. (Tech) Kirsi Holli-Helenius, for their support and feedback on the thesis. I would also like to thank Hannu Eskola for offering me this topic and all the guidance in the beginning of the work. I am grateful to Kirsi Holli-Helenius and Minna Sikiö for all the help and support during the work.

In Tampere, Finland, on 25 April 2016

Juho Pölönen

CONTENTS

LIST OF ABBREVIATIONS

ADC	Apparent diffusion coefficient
CAD	Computer aided diagnosis
CNR	Contrast-to-noise ratio
CP	Cerebral peduncle
DTI	Diffusion tensor imaging
DWI	Diffusion weighted imaging
FA	Fractional anisotropy
FID	Free induction decay
FOV	Field of view
MRI	Magnetic resonance imaging
MBR	Minimum bounding rectangle
NMR	Nuclear magnetic resonance
PD	Parkinson's disease
PET	Positron emission tomography
RF	Radio frequency
RN	Red nucleus
ROI	Region of interest
SE	Spin echo
SN	Substantia nigra
SNc	Substantia nigra pars compacta
SNr	Substantia nigra pars reticulata
SNR	Signal-to-noise ratio
SPECT	Single photon emission tomography

LIST OF SYMBOLS

γ	gyromagnetic ratio
μ_R	running mean
A	area
AR	aspect ratio
B	magnetic field strength
C	cluster centroid
D	diameter
f	frequency
f_{circ}	circularity
f_{comp}	compactness
f_{sol}	solidity
$f(x,y)$	image
$g(x,y)$	thresholded image
H	convex area
$h(x,y)$	histogram
M	magnetization
N	number of gray levels, number of pixels
n	gray level
P	perimeter
R	region
S	pattern
T	threshold point
T_{tol}	tolerance level
T1	longitudinal relaxation
T2	transverse relaxation
TE	time of echo
TR	time of repetition
X	sample

1. INTRODUCTION

Parkinson's disease (PD) is the second most common neurodegenerative disorder and it affects approximately 7 million people worldwide. PD is late life disorder and it is caused by degeneration of dopamine-producing cells in midbrain, which results in impairment of motor system. The most affected part of the midbrain is the substantia nigra where the loss is generally at least 50% of the dopaminergic cells [1, p. 10]. The disease progresses slowly and it causes bradykinesia, resting tremor, rigidity, postural reflex impairment and other movement-related symptoms [2, p. 1]. Many other disorders such as progressive supranuclear palsy, multiple system atrophy, corticobasal degeneration and dementia with Lewy bodies resemble PD, which makes the diagnosis challenging [3, p. 1].

Magnetic resonance imaging (MRI) is an imaging modality that uses magnetic field, radio waves and field gradients to form images of different organs and tissues within the body. It is based on a phenomenon called nuclear magnetic resonance (NMR) in which the nuclei of certain atoms absorb and release energy in amounts that are unique to those nuclei [4, p. 373]. MRI is one of the most applicable methods for structural brain imaging as it is relatively safe and sensitive to soft tissue pathologies. The current role of MRI (and other medical imaging modalities) in the diagnosis of PD is negligible, but it is advancing rapidly and it has potential to aid the understanding the disease mechanism and provide additional information in diagnosis process. Recent studies indicate that more advanced imaging and image processing methods can aid the diagnosis of PD [5][6][7].

Quantitative image analysis methods (e.g. shape analysis, texture analysis and morphometry) have been used for a variety of computer vision applications to detect changes that cannot be seen with human eye [8, p. 1-2]. However, the application to medical imaging is relatively new. Quantitative image analysis methods have mainly been used in computer aided diagnosis (CAD) systems to give supplementary information to radiologists [9]. The structural changes of midbrain in PD are rarely distinguishable by visual inspection of MR images. Quantitative shape analysis is a potential method to reveal these changes and improve the utility of MRI in the diagnosis of PD [10][11].

This Master's thesis was done at the Medical Imaging Centre of Tampere University Hospital and at the Department of Electronics and Communications Engineering of Tampere University of Technology. The aim of this thesis was to use quantitative shape analysis to study the differences in midbrain between PD patients and healthy controls. The study was limited to two brain structures: the substantia nigra pars reticulata and

the red nucleus. These brain structures were segmented from the axial brain MR images using three different image segmentation methods and several shape factors were calculated for each structure. The results were analyzed statistically using SPSS software.

Chapter 2 of this thesis gives a brief overview of PD, MRI and quantitative shape analysis. It also describes the required anatomical and pathophysiological details of the disease and how they can be detected using MRI and image analysis. Chapter 3 presents the material, methods and tools used in this thesis. The most important results of shape analysis and the different steps of image processing are presented in chapter 4. Chapter 5 contains the analysis of the results and chapter 6 concludes the thesis.

2. BACKGROUND

This chapter discusses the fundamental aspects of Parkinson's disease, magnetic resonance imaging and image analysis that are required to understand the essential parts of this work. At first, a general overview of Parkinson's disease is given and the necessary anatomy and pathophysiology are discussed further. The second part of this chapter introduces the theory of nuclear magnetic resonance and image formation in magnetic resonance imaging. The theory behind the image processing and analysis tools used in this work is presented in the last part of this chapter.

2.1 Parkinson's disease

Parkinson's disease affects approximately 7 million people worldwide and it is the second most common neurodegenerative disorder after Alzheimer's disease. It is still a relatively rare disease and it is more common in the elderly: the prevalence of PD is about 0.2-0.7% of the whole population and 1-3% of the people over 80 years in industrialized countries [2, p. 1-3]. The disease is about two times more common in men than in women, regardless of race or geographic location [2, p. 4].

PD is a chronic and progressive brain disorder that mainly affects the motor system. Overall, the disease affects the ability to initiate and maintain movement and it is classified as hypokinetic movement disorder [12, p. 2]. The disease itself is not fatal but it produces serious movement-related symptoms including rest tremor, rigidity, bradykinesia and impairment of postural reflexes. The rest tremor occurs as rhythmic, involuntary shaking of a limb while the muscles are relaxed. It does not occur during purposeful movement. The tremor typically begins only on one limb or one side of the body and it spreads gradually to all limbs [12, p.10]. Rigidity related to PD often occurs as soreness of arm or leg. It is caused by the failure of natural contraction and relaxation of opposing muscles. Bradykinesia occurs as general slowness and difficulty to perform repeated movements. It is generally present from the early stages of the disease and it causes major disability. Postural instability is also very disabling symptom and it occurs typically in the late stages of disease [12, p. 11-12].

PD involves the malfunction and death of the dopamine producing nerve cells in the basal ganglia which causes dopamine levels to decline over time. Loss of this neurotransmitter has been shown to cause most of the symptoms of PD [13, p. 1]. The most affected part of the basal ganglia is the substantia nigra where the loss is typically at least 50% of the dopaminergic cells [1, p. 10]. The cause of the cell death is unknown. Another abnormality in the substantia nigra is excess iron accumulation which is

thought to be associated with oxidative stress [14, p. 4]. Other changes in the substantia nigra are the depletion of tyrosine hydroxylase and the presence of Lewy bodies in the remaining nerve cells. Changes also occur in other structures including the locus ceruleus, the dorsal motor nucleus of the vagus, the hypothalamus, the nucleus basalis of Meynert and the sympathetic ganglia [1, p.10].

2.1.1 Anatomy of midbrain

The substantia nigra (SN) is a dark colored structure that is located in midbrain and is functionally connected to the basal ganglia. The basal ganglia is a group of nuclei that are associated with several movement related functions including starting, stopping and monitoring the movements executed by the cortex. The main part of basal ganglia consists of the caudate nucleus, putamen and globus pallidus [15, p.443]. The basal ganglia and its related structures are presented in Figure 2.1.

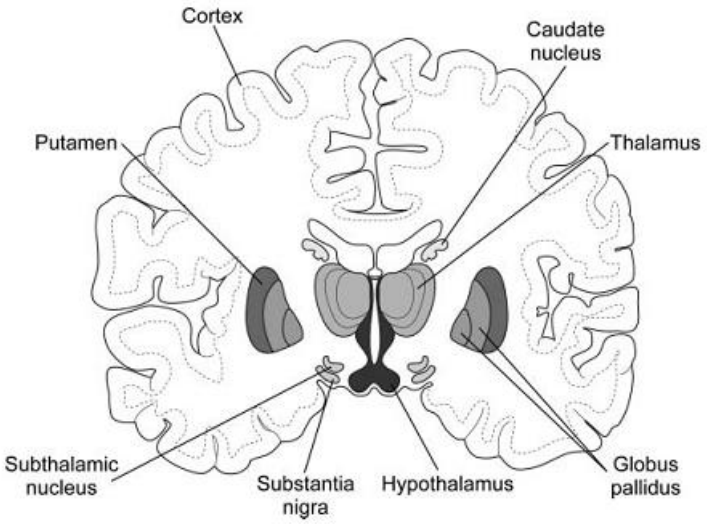

Figure 2.1 *The basal ganglia and related structures of the brain in coronal plane [12, p.6].*

The dark color of the substantia nigra is caused by high content of neuromelanin which is a precursor of dopamine [15, p.449]. In transverse plane, the SN is located in the dorsal side of the cerebral peduncle (CP) and on the ventral side of the red nucleus (RN). The red nucleus is an oval-shaped structure that is involved in limb coordination and reticular formation. Its red color is caused by its blood supply and by the iron pigment of its neurons [15, p. 449]. The anatomy of midbrain in transverse plane in is illustrated in Figure 2.2.

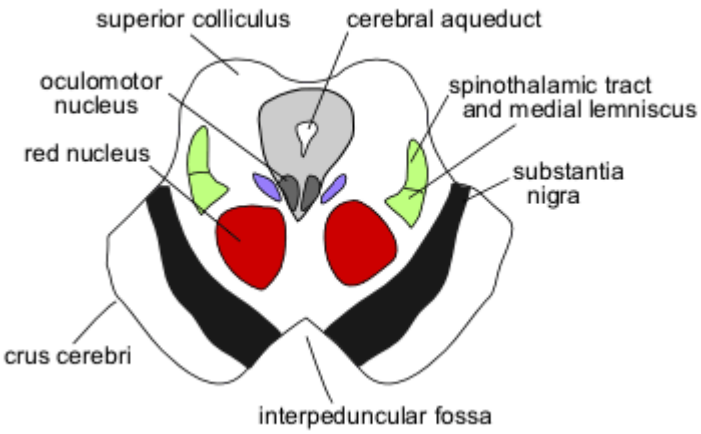

Figure 2.2 *Anatomy of midbrain in transverse plane [16].*

The SN is divided into two parts: the substantia nigra pars compacta (SNc) and the substantia nigra pars reticulata (SNr) [14, p. 3]. The SNr is the part of the SN that is connected to the CP and the SNc is located adjacent to the RN. These structures can be seen in a MR image of midbrain in Figure 2.3.

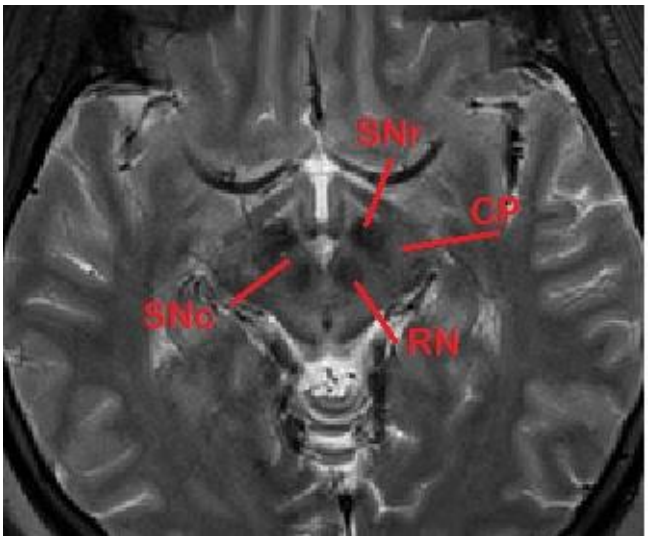

Figure 2.3 *T2 -weighted MR image of midbrain, SNc = substantia nigra pars compacta, SNr = substantia nigra pars reticulata, RN = red nucleus, CP = cerebral peduncle.*

SNc can be further divided into ventral and dorsal parts and both of these parts can be subdivided into three regions. These regions have found to possess significantly different concentrations of melanin. The loss of neurons in these regions is considerably different in PD than in normal aging. [14, p. 3]

2.1.2 Diagnostic methods

There are no standard clinical tests or imaging scans to diagnose PD. The diagnosis is performed based on the patient's medical history, signs and symptoms of PD and neuro-

logical and physical examinations [12, p. 16]. Making an accurate diagnosis is difficult, especially in the early stages of disease, because PD shares many symptoms with other neurological diseases. Diseases with most resemblance are progressive supranuclear palsy, multiple system atrophy, corticobasal degeneration and dementia with Lewy bodies. They are referred to as Parkinson-plus syndromes [3, p. 1].

Rest tremor, bradykinesia, gait and balance difficulties and dystonia are the most common signs of PD and they are observed in physical examinations. In addition, there are symptoms that are not related to movement. These include cognitive dysfunction, sleep disturbance, urinary incontinence, sexual dysfunction, depression and anxiety [12, p. 21-22]**.** The diagnosis typically requires several different tests and follow-ups so that Parkinson-plus syndromes and other diseases can be ruled out. One of the main features that help in diagnosis is that the signs and symptoms of PD are typically asymmetric (e.g. rest tremor appears only on one side of the body). Another feature is a sustained response to dopamine replacement medication (levodopa) and the significant improving of symptoms in PD [3, p. 9-10].

The current clinical applications of medical imaging such as ultrasound, positron emission tomography (PET), single photon emission tomography (SPECT) and magnetic resonance imaging (MRI) are not relevant to the diagnosis of PD but they are traditionally used to rule out other diseases. However, the research of advanced scanning and analysis procedures has shown promising results in diagnosis and pathophysiological understanding of PD [17][18][19].

2.1.3 Treatment

There is currently no cure for PD, but the symptoms can be relieved by physical therapy, occupational therapy, speech therapy, medical treatment and surgical treatment [12, p. 37]. Physical and speech therapies are used to improve and maintain motor and communicational skills and thus counter the symptoms of PD. Occupational therapy utilizes adaptive equipment, such as shower benches, grab rails, modified cutlery and long-handled shoehorns to help to maintain everyday routines despite the limitations [20, p. 221].

Dopamine replacement therapy is the oldest and most widely used medical treatment of PD. It involves a delivery of dopamine precursor called levodopa and inhibitor drug carbidopa. The purpose of carbidopa is to help levodopa cross the blood-brain barrier to brain where levodopa is converted to dopamine [21, p. 135]. Levodopa treatment typically helps to control the symptoms for 4 - 6 years with the least amount of side effects. However, many patients develop motor fluctuations, dyskinesia and other long-term complications with the medication [21, p. 134]. Other medications used in the treatment of PD include dopamine agonists, COMT inhibitors, monoamine, oxidase-B inhibitors, amantadine and anticholinergics [21, p. 137- 146].

Surgery is used generally to treat the most advanced cases of PD when the medical treatment is insufficient to relieve the symptoms. Three types of surgical methods are currently in clinical use: pallidotomy, thalamotomy and deep brain stimulation (DBS). Pallidotomy and thalamotomy involve a precise surgical destruction of certain parts of the brain structures that are affected by PD [12, p. 55]. DBS involves the implanting of a pacemaker-like device that generates electrical impulses to stimulate certain locations in the basal ganglia. This stimulation has proven to block the brain activity that causes the symptoms of PD [12, p. 56]. The device is typically implanted in the chest of the patient and it is connected to the midbrain through wires and electrodes. DBS is usually preferred over ablative surgery because the effect is not permanent and the stimulation can be adjusted afterwards.

2.2 Magnetic resonance imaging

Magnetic resonance imaging (MRI) is an imaging modality that uses magnetic field and pulsed radio frequency (RF) waves to form images of different tissues. It is based on a phenomenon called nuclear magnetic resonance (NMR) in which the nuclei of certain atoms absorb and emit electromagnetic radiation in a strong external magnetic field [4, p. 373]. MRI has superior soft tissue contrast compared to other imaging modalities. Consequently it is an effective imaging method to examine the brain structures and abnormalities. MRI is also considered relatively safe, since it does not use ionizing radiation. Although the current role of MRI in the diagnosis of PD is quite small, it is advancing rapidly and it has shown promising results in recent studies.

2.2.1 Nuclear magnetic resonance

The magnetic field strength in MRI imaging is typically between 0.1 and 4.0 T. A magnetic field of this magnitude causes protons to align with the applied field. Most of the protons align parallel to the field at low-energy state and the rest align anti-parallel to the field at a slightly higher energy state. This causes a measureable net magnetic moment in the direction of the magnetic field. The alignment of protons in an external magnetic field is presented in Figure 2.4.

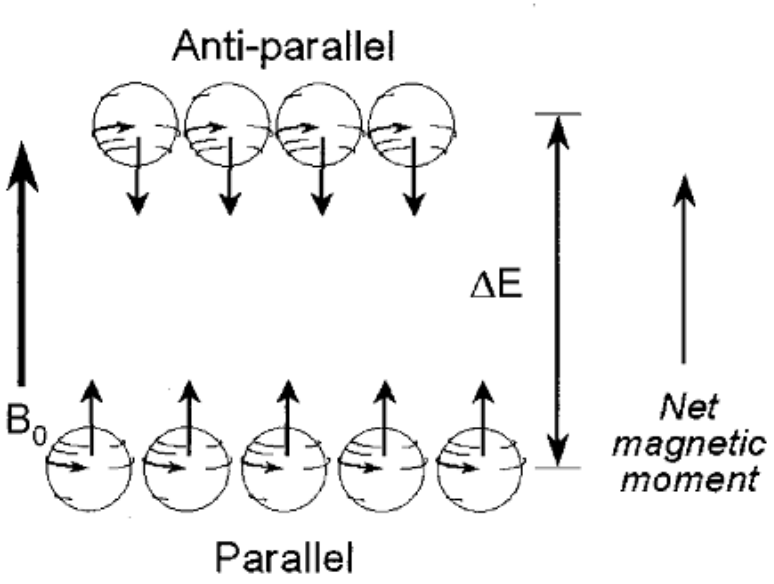

Figure 2.4 *Alignment of protons in an external magnetic field B_0 [4, p. 377]*

The magnetic field also causes a single proton to precess around its axis. The frequency of the precession f_0 can be described with the Larmor equation:

$$f_0 = \frac{\gamma}{2\pi} B_0, \tag{1}$$

where γ is the gyromagnetic ratio and B_0 is the magnetic field strength [4, p. 378]. The gyromagnetic ratio is unique to each element. Consequently, in a constant magnetic field the different elements can be discriminated based on their precession frequency.

At the equilibrium conditions the longitudinal magnetization in the direction of B_0 is maximal. There is no transverse magnetization because the protons are precessing in random orientation with respect to one another and the net effect is zero. When another magnetic field (B_1) precisely matched to the precession frequency of the protons is applied to the tissue, the protons begin to resonate and the net magnetization tips to the transverse plane. The magnetic field is introduced in a form of a RF pulse. When the energy of the RF pulse is absorbed and the protons begin to transition from parallel direction to anti-parallel direction the net longitudinal magnetization M_z changes from the positive maximum, through zero, to the negative maximum $-M_z$. The maximum of the transverse maximum M_{xy} occurs when there are equal numbers of parallel and anti-parallel protons and the longitudinal magnetization is zero. The angular displacement of the longitudinal magnetization vector is referred to as flip angle. A pulse with 90° flip angle provides the maximum transverse magnetization and 180° pulse results in the maximum negative longitudinal magnetization.

During the 90° pulse individual protons are phase coherent and M_{xy} rotates at the Larmor frequency. This produces a measureable sinusoidal signal. When the pulse ends, the phase coherence diminishes and the envelope of the sinusoidal signals begins to decay

exponentially. The resulting signal is called free induction decay (FID). A decaying M_{xy} -signal and the corresponding FID for a 90° pulse is illustrated in Figure 2.5. [4, p. 385-386]

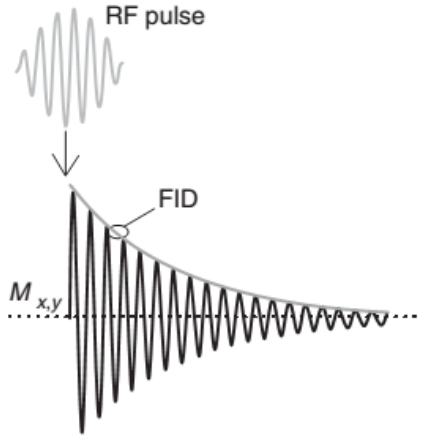

Figure 2.5 *Free induction decay (FID) of the transverse magnetization (M_{xy}) after a 90° RF pulse [22 p. 564].*

The time between the signal peak and 37% of the peak is referred to as T2 decay constant. Correspondingly, the T1 constant describes the relaxation time of longitudinal magnetization to equilibrium conditions. It is defined as the time required for longitudinal magnetization M_z to recover 63% of its initial value after the 90° RF pulse [4, p. 387]. Both T1 and T2 relaxation times depend heavily on the molecular properties of the material. Consequently, each tissue has rather unique relaxation times and it is the basis of contrast sensitivity in MRI.

The contrast is generated when the 90° and 180° RF pulses are fired in certain sequences to emphasize different tissues based on their relaxation times and proton density. One of the main pulse sequences is the spin echo (SE) sequence. In SE the 90° RF pulse is followed by a 180° pulse after a certain time. The 180° pulse inverts the spins and causes them to re-phase and produce an echo signal at the time of echo (TE). This procedure cancels out the effect of external magnetic field inhomogeneities [4, p. 391]. The spin echo pulse sequence is illustrated in Figure 2.6.

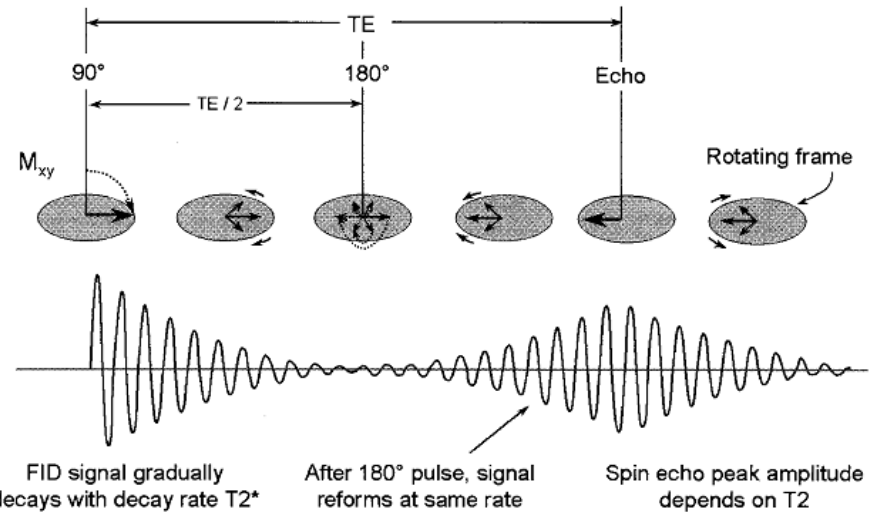

Figure 2.6 *The spin echo pulse sequence. FID = free induction decay, TE = time of echo [4, p. 392].*

The 90° pulses are fired in a series and the time interval between two consequent pulses is called the time of repetition (TR). The longitudinal magnetization recovers during this time delay and the output signal is recorded. In some applications the TR can also be set so that the longitudinal magnetization does not have time to recover and the tissue becomes partially saturated [4, p. 393]. The signal must be repeated hundreds of times to obtain the data for the image formation. The TE and TR parameters can be adjusted to emphasize either T1, T2 or spin density characteristics. For example, the typical T2 weighted sequence uses a TR of 1500-3500 ms and TE of 60-150 ms [4, p. 399].

2.2.2 MRI in Parkinson's disease

Several MRI studies with different imaging modalities have been conducted over the last decades to examine the structural changes of brain in PD. Some abnormal findings have been made in patients with PD, but the results have not been consistent enough for clinical use. Many of the findings have been in the substantia nigra region where the iron accumulation associated with PD occurs [14, p. 4]. An early study of Duguib et al. in 1986 showed that the width of SNc in axial T2 weighted images was significantly lower in patients than in controls [23]. Another study of Stern et al. in 1989 provided similar findings [24]. The narrowing of the SNc is sometimes detectable in MR images because iron causes strong signal loss in T2 -weighted MR images [14, p. 4]. This can be seen in Figure 2.3 where the naturally iron rich RN and SNr have low intensities.

The ultra-high field 7 T MRI is currently not in the clinical use, but it has been studied in a variety of medical applications including PD. Seven tesla imaging provides superior signal-to-noise ratio (SNR), contrast-to-noise ratio (CNR) and image resolution when compared to current 1.5 T and 3 T scanners. Therefore, it allows the depiction of smaller anatomical details and the earlier detection of lesions than the ordinary scanners [5].

The 7 T studies of PD have reported roughness of the boundary between the substantia nigra and crus cerebri [6]. This is illustrated in Figure 2.7. Another study revealed the absence of nigrosome-1 in the SNc in patients with PD [7].

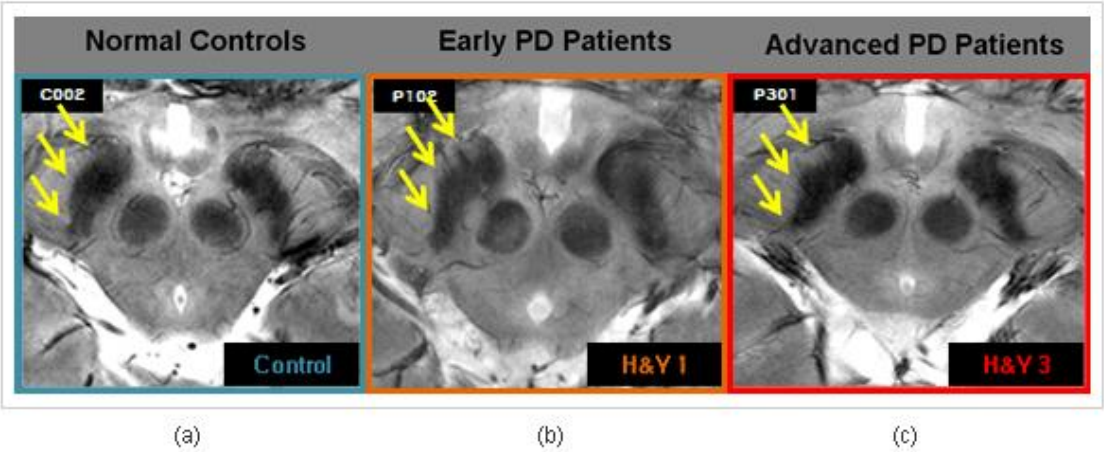

Figure 2.7 *Axial 7 T T2 weighted images of controls (a), early PD patients (b) and advanced PD patients (c). The arrows point to the differences in the boundary between the substantia nigra and crus cerebri [25].*

Changes in the substantia nigra have also been found with other structural MRI techniques. Hutchinson and Raff used a combination of two inversion recovery pulse sequences and detected a thinning of the substantia nigra in cases of PD [26]. MRI based volumetry was used by Krabbe et al. to identify regional volume changes associated with PD and MSA. They found out that the patients had significantly smaller volumes of substantia nigra than the controls [27]. Volumetry studies, especially voxel based morphometry, have also been used to detect changes in brain stem, striatum, thalamus, limbic system, frontal comples, temporal cortex and cerebellum in PD patients [19, p. 4-5].

Diffusion weighted imaging (DWI) and diffusion tensor imaging (DTI) are advanced imaging sequences that detect the diffusion of water molecules in tissues. DWI utilizes two strong subsequent gradient pulses to detect the movement of protons. The first pulse dephases the protons and the second rephrases them. If the location of the protons changes between the two pulses, a phase shift occurs and the recorded signal attenuates. In a free container the diffusion of water molecules is random and there is no net movement of the protons, but in biological tissues the random movement is constrained due to different cellular structures. In DWI this diffusion is quantified by calculation of apparent diffusion coefficients (ADC) for each voxel and the result is an ADC map that contains the magnitude of diffusion at each voxel but no directional information. Pathologies in brain cause local increases in the diffusion of water molecules, which results in increased ADC. However, some biological structures, such as brain fiber tracts allow diffusion only in one direction and this directional information is not shown by the ADCs. In DTI the directionality is quantified by deriving a tensor and a fractional

anisotropy (FA) value for each voxel. The results can be illustrated with a color coded tensor image, where the main direction of diffusion is presented with hue and the FA value with brightness. [14, p. 7][28, p. 88-89]

Both DWI and DTI have been used in many studies of the substantia nigra and its adjacent structures. The main findings are that the FA values in different parts of the substantia nigra are decreased in PD patients [29] and that the values correlate inversely with the clinical severity of PD [30]. The DTI study of Vaillancourt et al. yielded 100% sensitivity and specificity for distinguishing PD patients from controls when the FA values of the caudal substantia nigra were analysed [31].

2.3 Shape analysis

The general silhouette or shape is a primary visual feature in recognition of everyday objects by human beings as well as artificial objects in computer vision applications. In many cases, an object can be recognized only by its shape without any other pictorial features, such as color, texture, depth and motion. By the definition, shape of an object is all the geometrical information that remains after positional, rotational and scaling effects are filtered out [32, p. 1]. The goal of shape analysis is to represent or characterize this information using quantitative metrics. [8, p. 1-3]

Shape analysis has been one the most fascinating problems in computer vision and it has been used in a variety of applications including agriculture, visual arts, face recognition, surveillance, traffic control and medical diagnosis [8, p. 4-5]. In medical diagnosis, traditional shape analysis has always been in an important role as anatomical structures and abnormalities are often identified based on their shape. It is mainly used by radiologists to detect and monitor pathologies in medical images. In addition, quantitative shape analysis is used in computer aided diagnosis (CAD) systems. CAD systems are used by radiologists to detect and quantify pathologies in X-ray, MRI and ultrasound images and provide supplementary information to aid the diagnosis [9]. Quantitative shape analysis has also been used to study the effects of PD in MR images but it is not currently in clinical use. Hopes et al. used 3D shape analysis to study the atrophy of the striatum in PD patients together with volume analysis and determination of R2* values [33]. The study of Nemmi et al. revealed shape and volume differences in the putamen and the caudate nucleus. The shape changes also correlated with motor symptoms related to PD [11]. Kwon et al. used 7 T imaging and 3D shape analysis to study the shape and volume changes of substantia nigra in PD patients [6].

The shape analysis process involves several steps, most of which are related to enhancing the image and preparing it for the analysis itself. These preprocessing steps are often essential to achieve admissible results, especially if there are flaws during the image formation and the image quality is low. The next step after the preprocessing is the shape detection. It involves the locating the objects or regions of interest and their ex-

traction from the background. The shape detection is typically performed using automatic or semiautomatic image segmentation methods. In the final step, the shape characterization, quantitative metrics and representations are used to classify and analyse the extracted shapes. [8, p. 9-25]

2.3.1 Image preprocessing

Generally the objective of preprocessing is to correct defects and enhance the image so that it becomes more suitable for a specific application. One of the most common reasons to perform image preprocess is to make the image easier to visually examine and interpret. Many of the methods used in these kinds of procedures are based on the response of the human visual system. This makes them difficult to evaluate because the visual quality of the image is highly subjective and there is not a standard for a good result. Evaluating task is easier for methods that are based on the physics of light interactions and image generation. Another reason to preprocess the image is to prepare it for applications of machine perception (e.g., pattern recognition). In this case the preprocessing methods and algorithms can be easily evaluated based on the results of the machine perception application. In this work the purpose of preprocessing is to enhance the initial image to minimize errors and distortions in the manual and semiautomatic segmentation processes. [34, p. 269][35, p. 75-76]

The image preprocessing methods are divided into two vast categories: spatial domain methods and frequency domain methods. Spatial domain methods operate in the image plane and process individual pixels and their neighbourhoods. Pixel values are modified based on predetermined rules that depend on the original pixel values or they are compared to the values of neighbouring pixels. Frequency domain methods operate with the frequency domain transform (e.g., Fast Fourier Transform) of the original two-dimensional image. Their main use in image preprocessing is detecting and removing periodic structures from the image [34, p. 341]. There are also special techniques that utilize methods from both spatial domain and frequency domain [35, p. 75].

The image enhancement methods are fundamentally global and they modify pixel values based on the content of the entire image. For shape analysis purposes it is not optimal to process the entire image if we are only interested in a specific region. Hence the first step in the image preprocessing is to remove the excess image data by cropping the region of interest (ROI) from the original image. After the cropping the image contrast can be enhanced by histogram equalization. In histogram equalization the gray levels of the image are spread to a greater range of the grayscale while the individual pixels retain their intensity order. The new gray levels of the output image *f(n)* are mapped based on the histogram of the original image:

$$f(n) = (N-1)\sum_{k=0}^{n} h(k), \tag{2}$$

where *n* is the gray level in the original image, *N* is the maximum gray level and *h(k)* is the relative frequency histogram of the original image [8, p. 216-217]. After the transformation each pixel with gray level *n* is replaced by a gray level *f(n)* in the output image. Histogram equalization results in an image where it is possible to see variations within regions that appear nearly uniform in the original image. Not only this improves the visual quality of the image but also makes it easier to segmentation algorithms to distinguish objects from their background. An example of histogram equalization is presented in Figure 2.8.

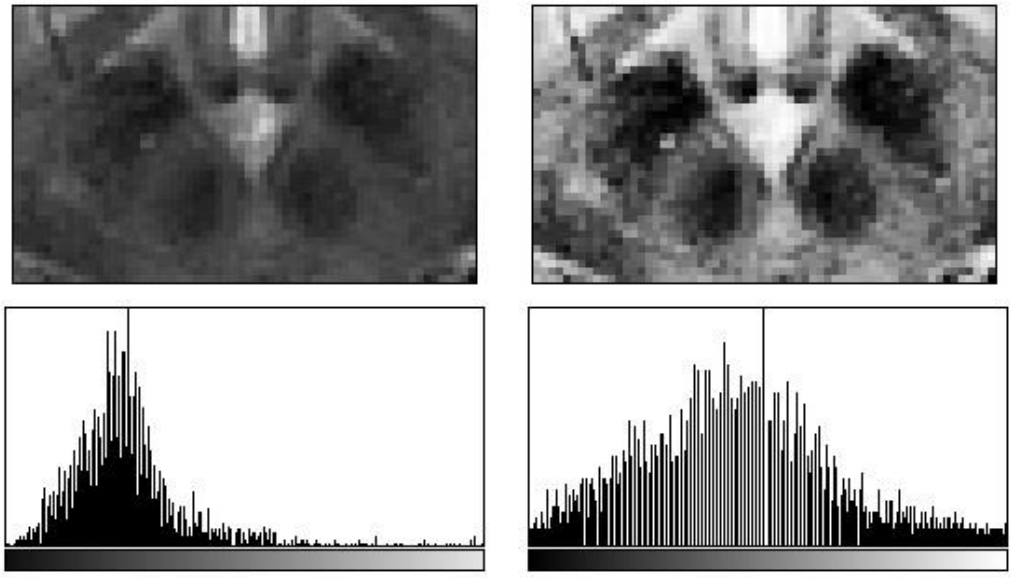

Figure 2.8 *Image and its histogram before (left) and after (right) the histogram equalization.*

Image noise can be reduced after the histogram equalization by filtering the image in spatial domain using a smoothing filter. Smoothing spatial filters fall into two categories: linear filters and order-statistic (or nonlinear) filters [35, p. 119-124]. Linear filters cause significant blurring and they are suitable for applications that include shape detection or counting. Order-statistic filters cause significantly less blurring than linear smoothing filters and they retain sharp edges in the image which makes them suitable for shape analysis and measurement applications [35, p. 123]. Median filtering is a classic order-statistic filtering technique and it is commonly used to eliminate impulsive noise [8, p. 228]. Median filter operates in a window and slides through the image pixel by pixel replacing each pixel with the median intensity value of its neighbourhood. Therefore single impulsive pixels are changed to be more like their surrounding pixels and large clusters are preserved. The window of the median filter is typically a square or circular (Figure 2.9) but other types of windows can be used as well.

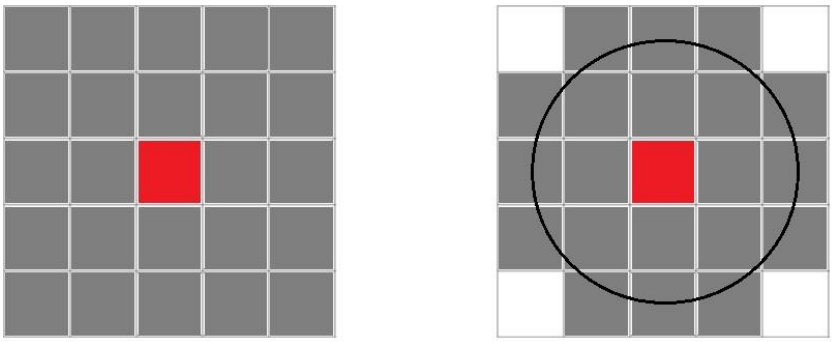

Figure 2.9 *A 5x5 sized square window and a circular window with radius of 2.*

The shape and size of the window affects the result significantly and the size should be selected according to the size of the smallest details in the image. For example, details whose area is less than one half the area of the window are replaced with the median of their neighbourhood [35, p. 124]. All window based operations encounter a special problem when the outermost pixels are processed near the image border and some parts of the window fall outside the image. There are three approaches to solve this problem:

1. The outside of the image is simply ignored and the window is not allowed to cross the image borders. Consequently, the resulting image is slightly smaller than the original.

2. Layers of pixels are added to the image borders so that the window remains full at the borders of the original image. The value of these added pixels is typically set to zero (zero-padding) or to match the value of the nearest border pixels. This method may cause distortions in the borders of the image.

3. The image is assumed to be periodic, so that when the window falls of the image, pixels from the other side of the image are used to fill it.

All of the above mentioned approaches are quite simple and easy to implement in the filtering algorithm. The right choice of the solution depends on each specific problem. [8, p. 219-220]

2.3.2 Image segmentation

Segmentation divides the image into regions of connected pixels with similar intensity values. In shape analysis applications the output of the segmentation process is typically a binary image, an image that consists of pixels with two possible intensity values: the pixels that belong to the object of interest (foreground) and the pixels that do not belong to the object (background) [36, p. 276]. Segmentation is one of the most challenging tasks in image processing and as mentioned before, the success is heavily dependent on the quality of the initial image. From the point of view of shape analysis, segmentation

accuracy is especially crucial since it has a direct effect on the results of the analysis algorithms.

There are three approaches to image segmentation: (1) thresholding or clustering, (2) boundary detection and (3) region growing [37, p. 226]. There are many different techniques based on these approaches, but in this thesis the focus is on three methods: manual thresholding, k-means clustering and seeded region growing.

Thresholding

Thresholding is a simple and widely used method for image segmentation. The fundamental idea is to split the histogram of an image *f(x, y)* into two parts so that the objects are separated from the background. This is done by selecting a threshold point *T* from between these regions. After the thresholding pixels for which $f(x, y) > T$ are segmented as object and the rest as background. Thresholded image *g(x, y)* is defined as

$$g(x,y) = \begin{cases} 1 & if\ f(x,y) > T \\ 0 & if\ f(x,y) \leq T. \end{cases} \quad (3)$$

In manual thresholding the threshold point is selected based on visual inspection of human operator. The threshold point can be determined straight from the histogram or interactively by observing the resulting image. There are also several automatic thresholding algorithms. [36, p. 42-44]

Histogram -based thresholding methods operate only with the intensity values ignoring the locational information and connectivity of pixels. Consequently, they are prone to local intensity inhomogeneities and impulsive noise. However, these weaknesses can be partially minimized by careful cropping and preprocessing. Also various morphological operations can be used to remove errors such as small particles and holes in the resulting binary image. Automatic thresholding methods are quick and they yield reproducible results but they only function under ideal lighting conditions and with high quality images. In many cases the intensity values of individual pixels are not uniquely related to the object and the threshold has to be set manually to produce an acceptable segmentation. However, the result of manual thresholding is based on the human visual system and it is not compatible with automatic methods. It is also time consuming, prone to human error and different results are likely to be produced at different times or by different operators. [34, p. 395-399]

Thresholding has been widely used in brain image analysis. Due to its simplicity, it is often used in conjunction with other segmentation methods. Abdulbaqi et al. developed a method for brain tumour detection that utilizes thresholding and Hidden Markov Random Fields [38]. Another brain tumour detection method was proposed by Natarajan et al. Their method is based on thresholding followed by morphological operations and image substraction [39]. Shanthi et al. developed a hybrid method of thresholding and

region growing for segmentation of white matter, gray matter and cerebrospinal fluid [40].

K-means clustering

In k-means clustering the image is segmented into *k* different clusters. The segmentation algorithm groups pixels with similar intensity values together and the resulting image consists of *k* different regions. The grouping is done by minimizing the sum of distances between pixel and the corresponding cluster centroids. The algorithm begins with the random selection of *k* initial cluster centroids in the histogram

$$C_1(1),\ C_2(1), \dots, C_k(1). \tag{4}$$

The second step is to assign each sample *X* to the nearest cluster depending on Euclidean distance using the relation

$$X\ \in\ S_j(i)\ if\ \left|X - C_j(i)\right| < |X - C_l(i)| \tag{5}$$

$$l = 1, 2, \dots, k; l \neq j$$

where $S_j(i)$ is the set of patterns with cluster centroid $C_j(i)$. In the third step, new clusters centroids are calculated as

$$C_j(i+1) = \frac{1}{N_j} * \sum X_j, \tag{6}$$

where N_j is the number of pixels who belong to the class with centroid C_j. The algorithm is completed if

$$C_j(i+1) = C_j(i), \tag{7}$$

otherwise it is repeated from step 2 until convergence is reached. [41]

K-means clustering algorithm is unsupervised and the only required input parameter is the number of clusters. It is also very efficient and easy to implement. The main drawbacks of k-means clustering are related to the cluster model. Clustering algorithms are not as robust as thresholding methods and they might even fail completely on some datasets. The algorithm also produces significantly different results with different values of *k* and locations of initial cluster centers [42, p. 453]. The proper *k* value is ambiguous and there are several methods to define it [43]. In simple image segmentation *k* can be defined iteratively by comparing the resulting images or using prior knowledge of the image. In the standard k-means clustering algorithm the initial cluster centroids are selected uniformly at random from the data points and it can sometimes lead to poor clustering. More sophisticated algorithms can be used to choose the cluster centroids more optimally. For example, an algorithm called k-means++ [44] utilizes weighted probabil-

ity distribution to choose the centroids for the standard k-means algorithm. K-means clustering is based only on the intensity values and it does not take pixel connectivity into account. For this reason the method shares some of the misclassification problems with thresholding methods.

K-means clustering is also a popular method in segmentation and classification of brain structures in MR images. Bhalerao et al. proposed a k-means clustering algorithm for segmentation of corpus callosum and its boundary [45]. Nair et al. used k-means clustering in their algorithm for estimating the volumes of white matter, gray matter and cerebrospinal fluid [41].

Region growing

Region growing methods groups adjacent pixels into regions according to predefined criteria. The procedure initiates typically from a set of one or more starting points called seeds [35, p. 613]. These seed points can be set inside the object either interactively or they can be pixels that fulfil certain criterion (e.g. pixels with certain intensity values) [36, p. 47]. The next step in the algorithm is to test every pixel adjacent to the seed points whether they are similar enough to belong to the same region. These connected pixels can be selected using two different principles; 4 -connectivity, where pixels are considered to be connected only to vertical and horizontal neighbours and 8-connectivity, where the diagonal neighbours are also included. The similarity criterion for testing pixels depends on the application and image data. For grayscale images the test can be based spatial properties such as textures and moments or it can compare absolute intensity values [8, p. 244][35, p. 613]. The basic intensity-based region growing algorithm examines each pixel *f(m, n)* connected to the seed point and adds them to the region if their absolute intensity level difference with respect to the seed point is within the predefined tolerance level T_{tol} [46, p. 398]

$$|f(m,n) - seed| \leq T_{tol}. \tag{8}$$

Each added pixel becomes a seed point for the next iteration and the algorithm continues until there are no more pixels to be added to the region and the object is filled. The problem with this simple approach is that it produces significantly different results for different seed points. A common approach to avoid this problem is to compare the neighbouring pixels with the mean gray level, called the running mean μ_{Rc} of the region at its current stage

$$\left|f(m,n) - \mu_{R_c}\right| \leq T_{tol} \tag{9}$$

where

$$\mu_{R_c} = \frac{1}{N_c} \sum_{(m,n)} \sum_{\in R_c} f(m,n), \tag{10}$$

where N_c is the number of pixels in the current stage R_c [46, p. 398]. This method is more likely to produce the same result for every possible seed point as long as the seed point is within the region.

The main advantage of region growing over clustering and thresholding algorithms is that it takes pixel connectivity into account and it can separate regions with similar properties. The algorithms are usually versatile and they allow the customization of selection criteria and even the selection of multiple criteria at the same time [46, p. 398-401]. Seeded region growing is a robust and easy-to-use method that allows relatively inexperienced operators to produce good segmentation results [47]. In addition, the higher level knowledge of image processing can be implemented through the selection of seed points. The main limitation of region growing methods is that they operate only with local information without the global view of the image. This limitation may become apparent in the formulation of a stopping rule when the region is ready and no more pixels satisfy the criteria. In other words the algorithm does not take the history of the growth in to account and it might not produce acceptable results with certain types of images. This problem can be countered by utilizing a priori information of the size and shape of the segmented region [35, p. 613]. Other drawbacks of the region growing methods are that they may not work on highly textured images and they are sensitive to noise [47].

Region growing has mainly been used in tumour detection in MR images. Ramya et al. developed a robust region growing algorithm for brain tumour detection in 2D MRI images [48]. Similar methods have also been proposed by Kavitha et al. [49] and Weglinski et al [50].

2.3.3 Shape factors

Shapes and contours can be described comprehensively using different quantitative representations and models such as skeletons and polygonal approximations [35, p. 644-650][46, p. 537-543]. However, in some applications it is desirable to present some properties of the shape in small dimensionless metrics, generally referred to as shape factors. Area, diameter and perimeter are simple and conventional examples of shape factors that describe mainly the size of the object. Correspondingly aspect ratio, circularity and compactness are factors that describe the overall shape. All algorithms used to calculate shape factors assume the input image to be strictly binary and the objects to be continuous. The shape factors can be calculated directly from the boundary points or, for example, using ellipse or rectangle fitting.

Minimum bounding rectangle (MBR) is a type of shape representation that encloses a finite geometrical shape into a smallest possible rectangle oriented to the x- and y- axes. It is typically specified by four coordinates: x_{min}, y_{min}, x_{max} and y_{max}. MBR is a simple tool that is used in many computational geometry applications and in spatial indexing

systems [51]. It describes the extents of the object and gives and approximation of the areal coverage. Shape based ellipse fitting produces an ellipse that best represents the boundary of the object. Several parameters can be extracted from the resulting ellipse including major axis, minor axis, angle and ellipticity [52]. It is a versatile representation that contains information about the shape and orientation of the object. MBR and ellipse fitting are illustrated in Figure 2.10.

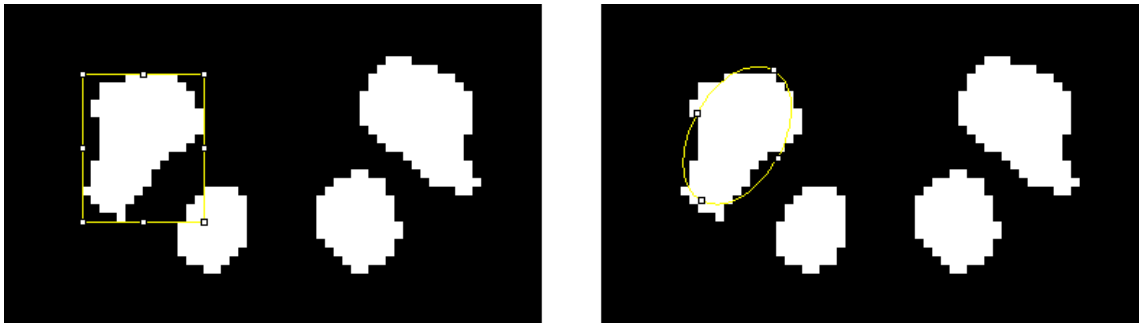

Figure 2.10 *Minimum bounding rectangle (left) and best fit ellipse (right) of the left substantia nigra pars reticulata.*

Aspect ratio of the object is calculated by fitting an ellipse to the boundary of the object along the x- and y- axes. It is defined as the ratio of the major axis of the ellipse to its minor axis and it describes the eccentricity of the shape [46, p. 551]. The inverse of the aspect ratio is defined as roundness.

Feret's diameter or caliper diameter is the longest distance between any two points on the boundary. It gives a more accurate estimation of the maximal length of the object than the parameters derived from the MBR or best fit ellipse. Correspondingly, the minimum Feret's diameter defines the width of the object [34, p. 589].

Circularity is one of the most generally used shape factors. It describes the elongation of the object and it is also a very sensitive indicator of boundary irregularities. Circularity f_{circ} is defined as

$$f_{circ} = \frac{4\pi A}{P^2}, \tag{11}$$

where A is the area and P is the perimeter of the object [34, p. 600]. The circularity of a perfect circle is 1 and as the elongation increases the value approaches zero. The reciprocal of circularity is used to describe general irregularity of the shape. Compactness f_{comp} is another metric that describes the deviation from a circular shape. It is defined as

$$f_{comp} = \frac{\sqrt{\frac{4}{\pi}A}}{D_{max}}, \tag{12}$$

where D_{max} is the maximum diameter of the object [34, p. 600]. Compactness increases both with eccentricity and elongation of the shape [36, p. 282-283].

Solidity describes the convexity or concavity of an object. It is defined as

$$f_{sol} = \frac{A}{H}, \tag{13}$$

where H is the convex area of the object [34, p. 600]. Convex area is the area of the convex hull of the object and its calculation requires more sophisticated algorithms. Typically the convex hull is constructed using several iterative dilation and erosion steps but they are not suitable for small object in a square pixelated grid. More suitable method to construct the convex hull is the so called rubber-band method [34, p. 586]. It involves the rotation of the coordinate axes and locating the minimum and maximum points at a series of rotational angles. The result is a n-sided polygon that surrounds the object and it effectively defines its convex area. The solidity of a perfectly convex shape is 1. Example values of aspect ratio, circularity and solidity are presented in Figure 2.11.

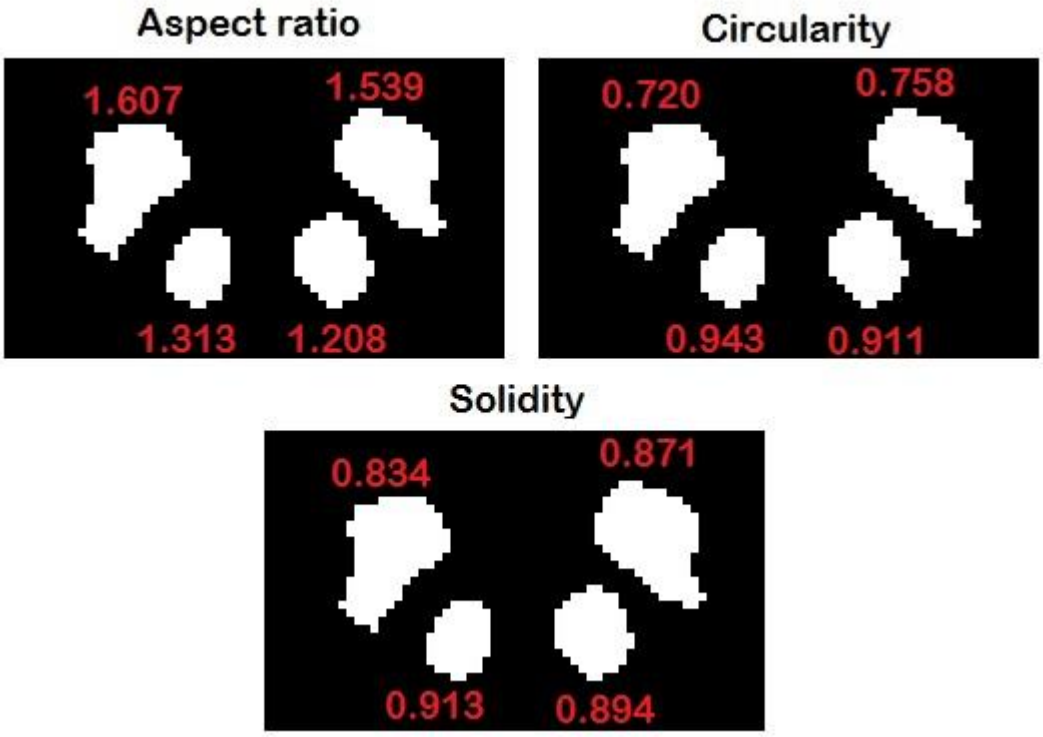

Figure 2.11 Aspect ratio, circularity and solidity values for substantia nigra pars reticulata and red nucleus in a segmented image of midbrain.

Depending on the application, there are some properties considering the efficiency and versatility of the shape factor. Invariances to shift in spatial position and scaling are essential for most application. In addition, for some applications rotation and reflection invariances are also required [46, p. 549].

Shape factors are combinations of size parameters which makes them prone to measurement inaccuracies and distortions in the image. They can also be inaccurate with very low image resolutions as the boundaries of the objects become pixelated. Another limitation is that they are not unique and they carry only a limited amount of information about the original shape. These limitations are problematic, especially for identification purposes, as several visually different shapes can have exactly the same value for a certain shape factor. This non-uniqueness is illustrated in Figure 2.12. However, the variations of different shape factors are independent. Due to these reasons shape should be analyzed using several different shape factors. Because the information of a single shape factor is very limited, the shape factors have to be selected so that they bear relationship to the presumed changes in the measured object. The appropriate combination of the shape factors depends entirely on the application. In shape identification and classification applications the shape factors can be easily defined beforehand and the amount depends on the complexity of the shapes. The selection of shape factors can be challenging in applications considering detection of unpredictable changes and thorough comparison of shapes. [34, p. 599-602]

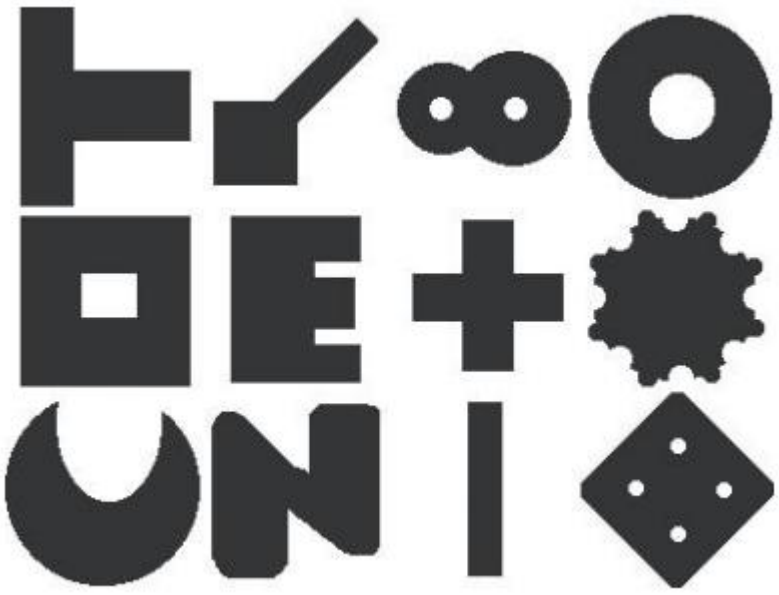

Figure 2.12 *A set of visually distinct shapes that have identical circularity values (f_{circ} = 0.44) [34, p. 601].*

3. MATERIAL AND METHODS

This chapter introduces the material, methods and software used in the image analysis process of this work. The different steps of the image analysis process (preprocessing, segmentation and shape analysis) are discussed in the same order as in the previous chapter.

3.1 Patients and controls

The study group consisted of 29 patients (aged between 42 - 86, mean age 67.6 ± 10.6 years, 12 males, 17 females) with symptoms of PD. The exclusion criteria were Alzheimer's disease or other dementia, cardiac, lung or gastrointestinal disease, kidney or liver malfunction, active malignant neoplasm, neurological or psychiatric disease, contra indication for MRI, alcohol or drug addiction and gravidity. The control group was selected using the same criteria and it consisted of 20 healthy volunteers (aged between 58 - 80, mean age 65.4 ± 6.8 years, 4 males, 16 females).

3.2 MRI acquisition

MR images were acquired in Tampere University Hospital using a 3 T MRI device (Siemens Trio, A Tim System, Siemens Healthcare Sector, Erlangen, Germany) with a 12-channel head matrix coil under standardized clinical protocols. The images used in this study were from T2-weighted three-dimensional sampling perfection with application-optimized contrasts using different flip angle evolution (SPACE) series with the following parameters: TR=3200 ms, TE=354 ms, Slice/gap 3.0/0 mm/mm, Matrix size=384x290 pixel, FOV=230 mm, flip angle=120°.

3.3 Image preprocessing

Image processing was performed using ImageJ image processing and analysis software (version 1.48v) [53]. ImageJ is an open source Java-based image processing program that can be used to process 8-bit, 16-bit and 32-bit images. It supports several image formats including TIFF, GIF, JPEG, BMP, DICOM, FITS and raw image data. ImageJ is highly customizable and there is a variety of plugins, toolboxes and related third-party software available for it [53].

The preprocessing of images used in this work was performed using the standard tools of ImageJ. At first, the axial brain images were cropped by manually placing a 62x37

pixel *Rectangular selection* over the midbrain so that the brain structures of interest were enclosed in it. The size was selected so that it was enough to contain the brain structures in every image. Next the image histogram was equalized using the *Enhance Contrast* -tool. The amount of pixels that were allowed to become saturated was set to 0.4%. After the contrast enhancement the image was filtered using a median filter with a radius of 2 pixels. ImageJ utilizes circular windows for all median, mean, minimum, maximum and variance filters and it assumes that out-of-image pixels have a value equal to the nearest edge pixel [54]. The cropping and the preprocessing settings are presented in Figure 3.1.

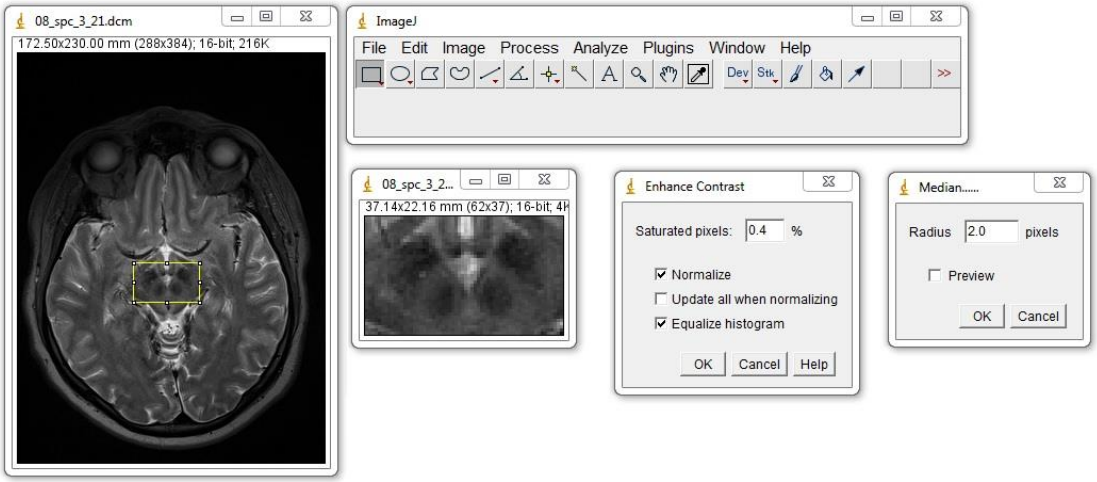

Figure 3.1 The user interface of ImageJ with a sample image, cropped image and settings for *Enhance Contrast* and *Median Filter* -tools.

The *Macro Recorder* -tool was used to create macros for the above-mentioned processes to streamline the processing of the rest of the images. The rectangular selection was performed using the following macro

```
makeRectangle(108, 196, 62, 37);
```

After that the rectangular selection was placed manually over the brain structures and cropping, contrast enhancement and filtering were performed using the macro:

```
run("Crop");
run("Enhance Contrast...", "saturated=0.4 normalize equal-
ize");
run("Median...", "radius=2");
```

3.4 Image segmentation

The preprocessed images were segmented using three different methods: thresholding, k-means clustering and seeded region growing. Most of the segmentation was done using ImageJ but MATLAB was also used to perform the seeded region growing. In a few images some of the regions had to be filled manually after the segmentation and some distinct pixels had to be removed.

Thresholding was implemented using the *Threshold*-tool of ImageJ and by manually adjusting the threshold. Thresholding was performed manually, because none of the automatic thresholding tools of ImageJ produced acceptable results. The threshold was selected so that the both RNs and SNrs were segmented and there were no connections between them in the binary image. Any excess regions were erased from the image. The view of the *Threshold*-tool is presented in Figure 3.2.

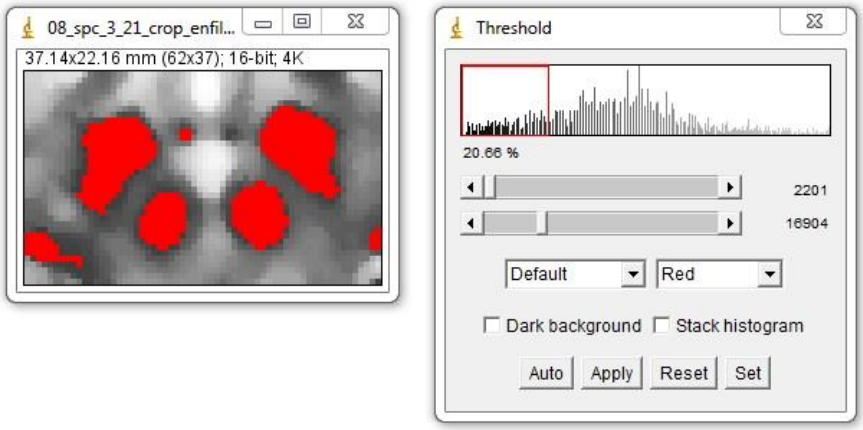

Figure 3.2 The *Threshold* -tool of ImageJ. The segmented regions are presented with red color.

The k-means clustering was also performed using ImageJ and the segmentation plugin of ij-Plugins Toolkit [55]. The plugin utilizes k-means++ algorithm to choose the initial seeds for the segmentation [55]. The settings were set as default (Number of clusters=4, Cluster center tolerance=0.0001, Enable randomization seed, Randomization seed=48) but the number of clusters was increased from four to five or six when the RNs and SNrs could not be distinguished in the resulting image. However, this procedure was only required for a few images. In this application the aim of the k-means clustering was to get the RNs and SNrs within the same cluster and hence isolate them from the background. The configuration window and settings for k-means clustering -tool are presented in Figure 3.3.

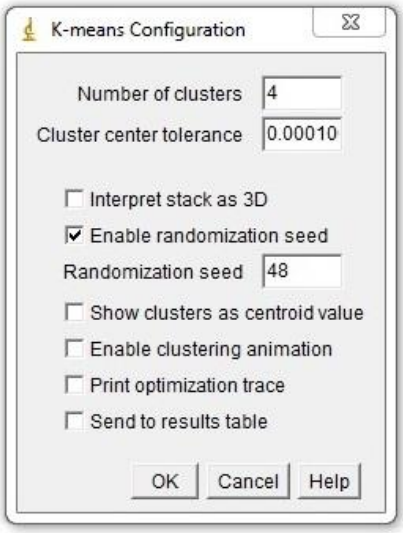

Figure 3.3 The settings for k-means clustering tool of ij-Plugins Toolkit.

The configuration was done for the majority of the images using the following macro:

```
run("k-means Clustering ...", "number_of_clusters=4 clus-
ter_center_tolerance=0.00010000 enable_randomization_seed
randomization_seed=48");
```

MATLAB (version 8.5) and Fast 3D/2D Region Growing -algorithm [56] was used to segment the image using seeded region growing method. The stopping criterion of the algorithm is that there are no pixels in the region's 4-connected neighbourhood that have an intensity difference smaller than the defined maximum intensity difference to the region's mean intensity [56]. The segmentation was initiated using a MATLAB -command:

```
lMask = RegionGrowing(dImg, dMaxDif, iSeed);
```

where *lMask* is the result of the segmentation, *dImg* is the original image, *dMaxDif* is the maximum intensity difference and *iSeed* is the seed point [56]. If the seed point is not provided, a GUI will open and the seed point can be select using the cursor.

The maximum intensity difference was initially set to 3000 and the seed points were set manually inside the RNs and SNrs using the simple GUI of the algorithm. The resulting image was inspected visually and in some cases the maximum intensity difference had to be increased to achieve acceptable segmentation. Also some structures had to be filled manually because single impulsive pixels inside the structures were not included in the region.

3.5 Shape analysis

The shape factors were calculated using the *Measure* -tool of ImageJ. The following measurements were selected at the *Set Measurements* -window: Area, Bounding rectangle, Shape descriptors, Perimeter, Fit ellipse and Feret's diameter. Each of the measurements included several shape parameters. The measurements yielded altogether 18 parameters, 13 of which were selected for further analysis. The selected parameters are listed with descriptions in Table 1. The excluded parameters were inverse values or coordinates that have no use in the shape analysis. The complete list of parameters is presented in Appendix 1.

Table 1 ImageJ shape parameters and their descriptions [57].

Parameter	**Description**
Area	Area of selection in selected units
Perim.	Perimeter, the length of the boundary
Width	Width of the bounding rectangle
Height	Height of the bounding rectangle
Major	Primary axis of the best fitting ellipse
Minor	Secondary axis the best fitting ellipse
Angle	Angle between the primary axis of the best fitting ellipse and a line parallel to the X-axis of the image
Circ.	Circularity. See equation 11
Feret	Feret's diameter. The maximum diameter of the object
FeretAngle	The angle of Feret's diameter
MinFeret	The minimum diameter of the object
AR	Aspect ratio
Solidity	Solidity, see equation 13

The measurements were conducted for each structure (lRN, rRN, lSNr and rSNr) and one at the time. The measured structure was selected using the *Wand (tracing)* -

selection tool which could also be used with k-means clustering images that were not binary images. The results were exported into an xls-file for further analysis. The process was repeated for each of the three segmentation methods and it yielded 12 datasets in total.

3.6 Statistical analysis

All the resulting datasets were analyzed statistically with the Mann-Whitney U test to find out whether there were significant differences between the patients and the controls. *P*-values less than 0.05 were considered statistically significant. The statistical analysis was performed using SPSS software (version 23.0.0). It was also used to create the boxplots of the statistically significant results.

4. RESULTS

The shapes of the red nucleus and the substantia nigra pars reticulata were analysed from T2 -weighted axial MR -images of midbrain. The analysis was performed for both the left and the right hemisphere. The main part of this chapter introduces the shape analysis results for the each of the four brain structures. The comparison table of the results for all shape factors, segmentation methods and brain structures is presented in Appendix 2.

4.1 Image preprocessing and segmentation

After determining the ROI the image was cropped, histogram equalization was performed and the image was filtered using a median filter. The preprocessing steps are illustrated in Figure 4.1.

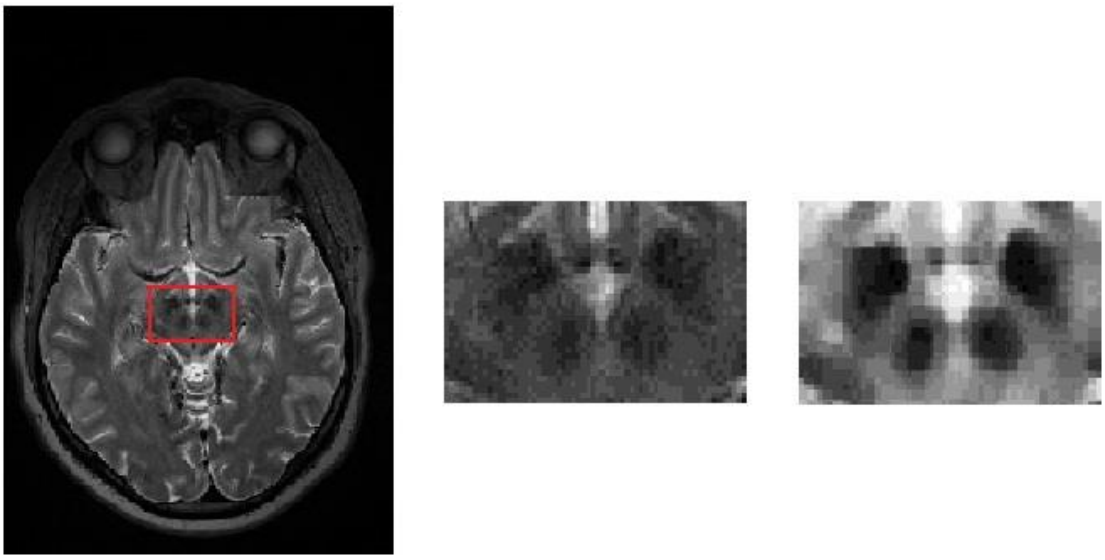

Figure 4.1 *An example image at the different preprocessing steps*: *the initial image with the rectangular selection (left), cropped image (center), and enhanced and filtered image (right).*

The enhanced and filtered image was then segmented using thresholding, region growing and k-means clustering. The resulting images of thresholding and region growing are binary images but k-means clustering produces an image that contains 4, 5 or 6 different intensity levels, one for each cluster. The segmentation results of the image in Figure 4.1 are presented in Figure 4.2.

Figure 4.2 *The preprocessed image in Figure 4.1 segmented with three different methods: thresholding (left), region growing (center) and k-means clustering (right)*

The above-mentioned steps were conducted for all of the patient and control images. In some cases the segmentation did not succeed and at least some of the structures were left out from the resulting image. In these cases the segmentation parameters were adjusted as described in Section 3.3 and the segmentation was repeated. In some rare cases the image had to be excluded because an acceptable segmentation could not be achieved. Three examples of discarded images are presented in Figure 4.3.

Figure 4.3 *Three problematic images that were excluded from the material. The images have been preprocessed.*

The problem with leftmost image in Figure 4.3 was that the SNc and RN could not be distinguished and they segmented as one region. In the centermost image the contrast is weak on the right hemisphere and the RN could not be segmented. In the third image the low intensity area between the RNs connected to the right RN. The total number of discarded images was nine for region growing and k-means clustering segmentations. Thresholding was successful with all of the images.

4.2 Shape analysis of the red nucleus

The analysis was performed for both the left (lRN) and the right red nucleus (rRN) with all three segmentation methods. Thresholding and region growing segmented images did not produce significant statistical difference between the patients and the controls. The only exception is the aspect ratio (*AR*) of lRN in the region growing segmented images. The p-values of the shape factors calculated from thresholding and region growing segmented images are presented in Table 2 and Table 3.

Table 2 *The p-values of the red nucleus (RN) shape factors between patients and controls calculated from thresholding segmented images. The shape factors are explained in Appendix 1.*

Shape factor	Left RN	Right RN
Area	0.469	0.513
Perimeter	0.661	0.436
Width	0.214	0.970
Height	0.226	0.247
Major	0.579	0.559
Minor	0.817	0.627
Angle	0.679	0.520
Circ.	0.562	0.382
Feret	0.502	0.987
FeretAngle	0.721	0.871
MinFeret	1.000	0.484
AR	0.377	0.711
Solidity	0.440	0.394

Table 3 *The p-values of the red nucleus (RN) shape factors between patients and controls calculated from region growing segmented images. Statistically significant ($p < 0.005$) values are bolded. The shape factors are explained in Appendix 1.*

Shape factor	Left RN	Right RN
Area	0.670	0.451
Perimeter	0.642	0.434
Width	0.580	0.611
Height	0.300	0.654
Major	0.483	0.757
Minor	0.623	0.619
Angle	0.799	0.654
Circ.	0.355	0.494
Feret	0.614	0.804
FeretAngle	0.443	0.788
MinFeret	0.612	0.520
AR	**0.041**	0.684
Solidity	0.799	0.486

However, the analysis of k-means clustering images showed significant difference in several shape factors between the two groups. The differences are mainly in the shape factors calculated from the lRN. The p-values of shape factors calculated from k-means clustering segmented images are presented in Table 4. The shape parameters with statistically significant differences are presented as box plots in Figure 4.4.

Table 4 *The p-values of the red nucleus (RN) shape factors between patients and controls calculated from k-means clustering segmented images. Statistically significant ($p < 0.005$) values are bolded. The shape factors are explained in Appendix 1.*

Shape factor	Left RN	Right RN
Area	**0.048**	0.334
Perimeter	**0.042**	0.230
Width	0.447	0.283
Height	**0.016**	0.264
Major	**0.034**	0.149
Minor	0.359	0.486
Angle	0.549	0.946
Circ.	**0.047**	**0.042**
Feret	**0.026**	0.213
FeretAngle	0.769	0.918
MinFeret	0.324	0.487
AR	0.112	0.482
Solidity	0.801	0.832

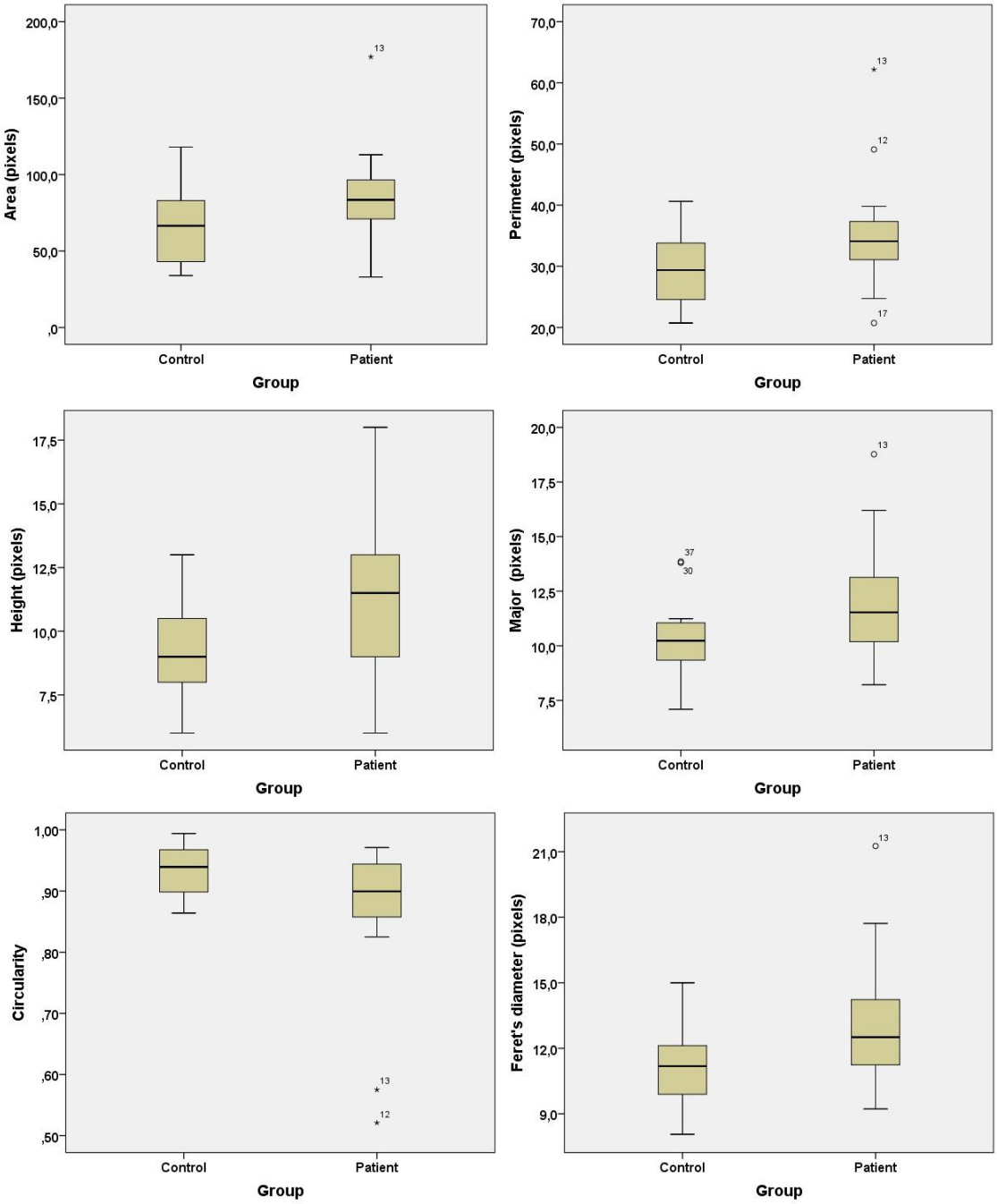

Figure 4.4 *Box plots for area (top left), perimeter (top right,), height of the bounding rectangle (center left), major axis of the best fitting ellipse (center right), circularity (bottom left) and Feret's diameter (bottom right) of the left red nucleus calculated from k-means clustering segmented images.*

Area, Perimeter, Height, Major and Feret's diameter in Figure 4.4 all indicate that the overall size of the lRN is greater in the patient group. Correspondingly lower circularity suggests that the shape of the lRN is more irregular among the patients. As it can be seen in Table 4, the results are quite different for the right hemisphere. The only parameter that shows significant difference in rRN is the circularity.

4.3 Shape analysis of the substantia nigra pars reticulata

The left (lSNr) and the right substantia nigra pars reticulata (rSNr) were analysed following the same procedures as above. Similarly to the RN analysis, there were differences only in the k-means clustering images and the differences were substantially greater in the left hemisphere. In this case there were barely any statistical differences in the parameters of right hemisphere. The p-values of shape factors calculated from thresholding and region growing segmented images are presented in Table 5 and Table 6.

Table 5 *The p-values of the substantia nigra pars reticulata (SNr) shape factors between patients and controls calculated from thresholding segmented images. The shape factors are explained in Appendix 1.*

Shape factor	Left SNr	Right SNr
Area	0.416	0.200
Perimeter	0.219	0.315
Width	0.582	0.703
Height	0.307	0.493
Major	0.253	0.369
Minor	0.782	0.474
Angle	0.136	0.461
Circ.	0.154	0.743
Feret	0.207	0.350
FeretAngle	0.092	0.259
MinFeret	0.836	0.661
AR	0.229	0.694
Solidity	0.316	0.713

Table 6 *The p-values of the substantia nigra pars reticulata (SNr) shape factors between patients and controls calculated from region growing segmented images. The shape factors are explained in Appendix 1*

Shape factor	Left SNr	Right SNr
Area	0.623	0.566
Perimeter	0.525	0.410
Width	0.837	0.412
Height	0.389	0.564
Major	0.284	0.406
Minor	0.860	0.961
Angle	0.500	0.439
Circ.	0.362	0.494
Feret	0.261	0.357
FeretAngle	0.901	0.062
MinFeret	0.642	0.852
AR	0.661	0.255
Solidity	0.138	0.585

The p-values of shape factors calculated from k-means clustering segmented images are presented in Table 7. The box plots for shape factors with statistically significant p-values are presented in Figure 4.5 and Figure 4.6.

Table 7 *The p-values of the substantia nigra pars reticulata (SNr) shape factors between patients and controls calculated from k-means clustering segmented images. Statistically significant ($p < 0.005$) values are bolded. The shape factors are explained in Appendix 1.*

Shape factor	Left SNr	Right SNr
Area	**0.029**	0.875
Perimeter	**0.007**	0.918
Width	0.198	1.000
Height	**0.039**	0.918
Major	0.051	0.881
Minor	0.101	0.817
Angle	**0.012**	0.593
Circ.	**0.012**	0.590
Feret	**0.024**	0.918
FeretAngle	**0.015**	0.424
MinFeret	**0.014**	0.886
AR	0.486	0.613
Solidity	**0.047**	0.416

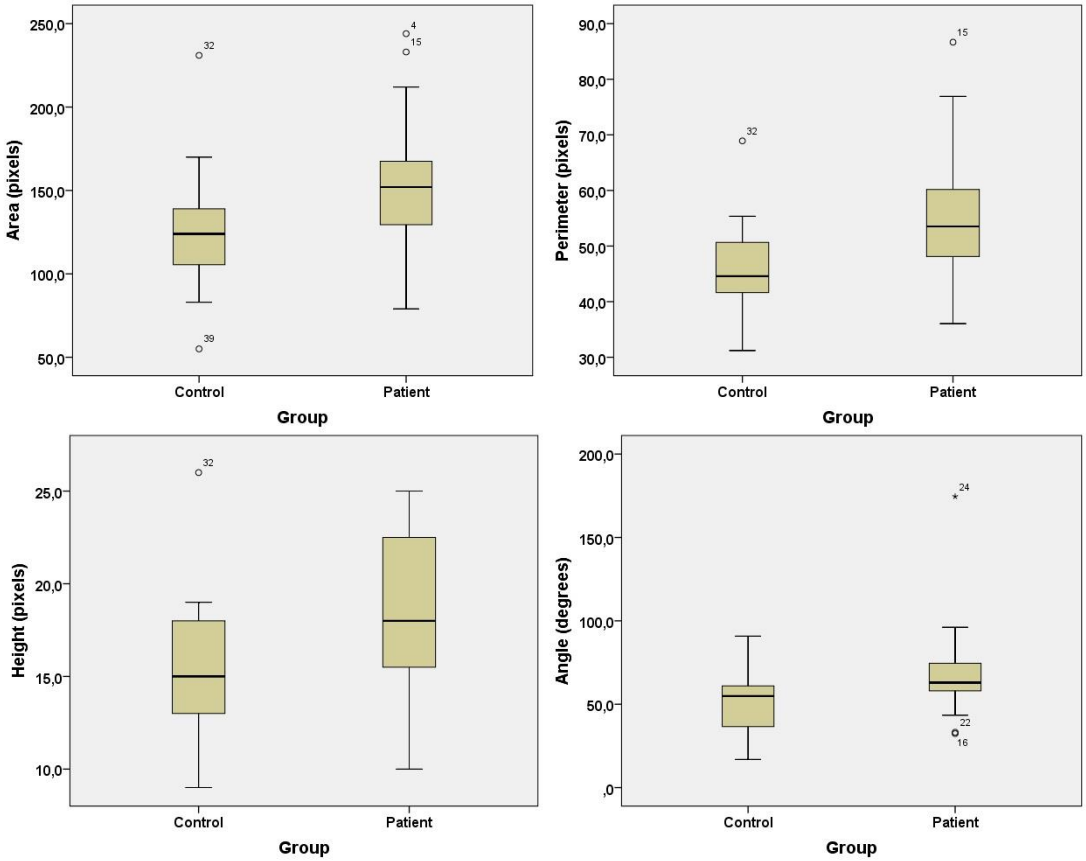

Figure 4.5 *Box plots for area (top left), perimeter (top right), height of the bounding rectangle (bottom left) and angle of the best fit ellipse (bottom right) of the left substantia nigra pars reticulata calculated from k-means clustering segmented images.*

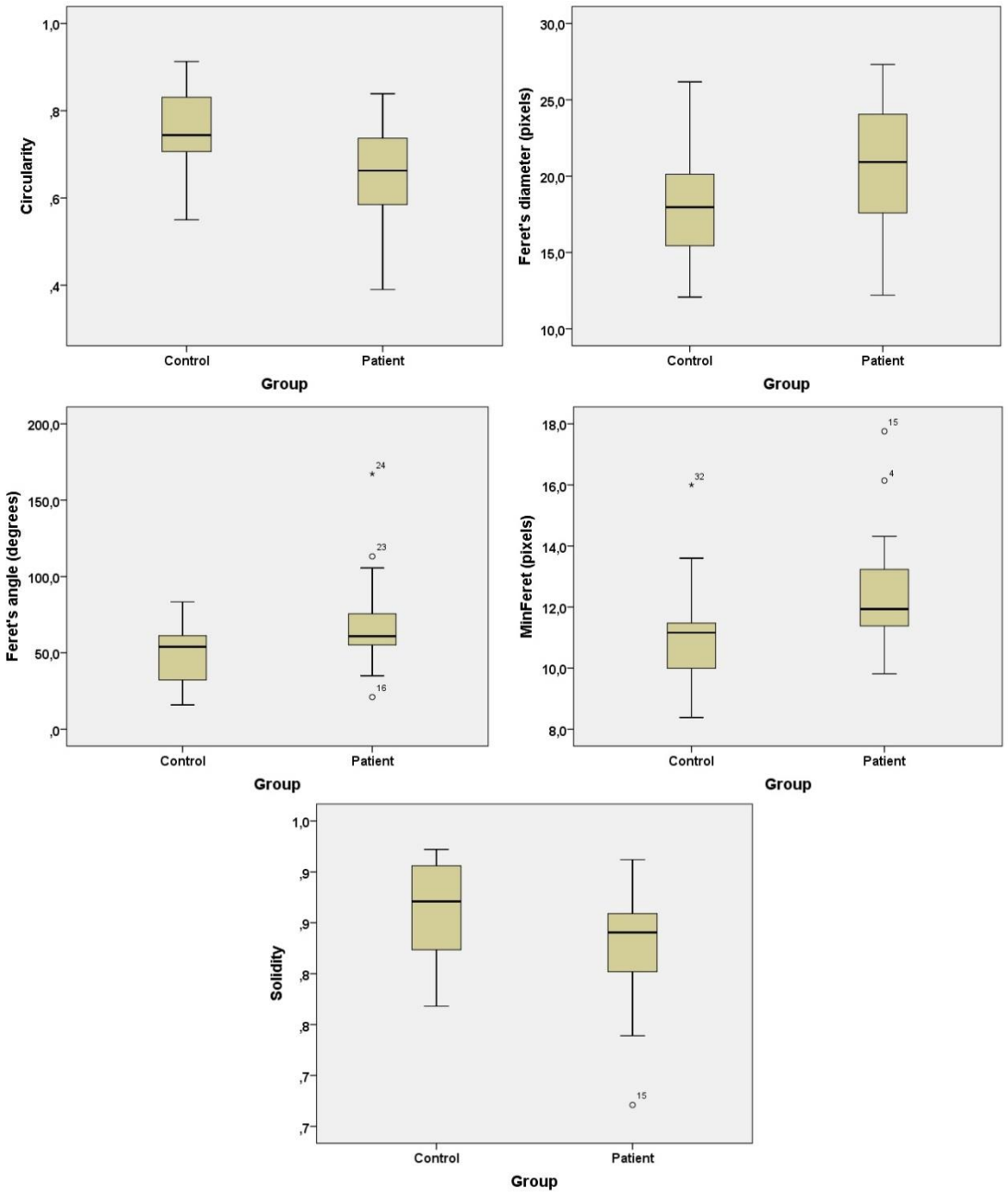

Figure 4.6 *Box plots for circularity (top left), Feret's diameter (top right), angle of the Feret's diameter (center left), the minimum Feret's diameter (center right) and solidity (bottom) of the left substantia nigra pars reticulata calculated from k-means clustering segmented images.*

As the Table 7 shows, there are clear differences in most of the parameters in the left hemisphere but in the right hemisphere there is barely any distinction. It can be seen in the Figure 4.5 and Figure 4.6 that the overall size of the lSNr is greater in the patient group and the circularity is smaller. The increase of size and the decrease of circularity could also be observed in the RN analysis, but in this case also the solidity and the angular parameters (Angle and FeretAngle) show difference between the two groups. This

is due to more complex and non-circular shape of the SNr. The main results of the shape analysis are concluded in Table 8.

Table 8 *The conclusion of the shape analysis results of k-means clustering segmented images. The shape factors are explained in Appendix 1.*

Shape factor	Left RN	Left SNr
Area	Increased in patients	Increased in patients
Perimeter	Increased in patients	Increased in patients
Height	Increased in patients	Increased in patients
Major	Increased in patients	No significant difference
Angle	No significant difference	Increased in patients
Circ.	Decreased in patients	Decreased in patients
Feret	Increased in patients	Increased in patients
FeretAngle	No significant difference	Increased in patients
MinFeret	No significant difference	Increased in patients
Solidity	No significant difference	Decreased in patients

5. DISCUSSION

Only one of the three sets of segmented images provided statistically significant differences between the patients and the controls. However, these findings correlate with current pathophysiological and anatomical knowledge of PD. In this chapter the results presented in the previous chapter are discussed further. Image segmentation proved to have a great impact on the final results and for that reason each segmentation method and their results are evaluated and discussed individually before the results of shape analysis. Also the main limitations of the used methods and the probable sources of error are considered.

5.1 Image segmentation

Image segmentation was expected to be the most critical phase in the analysis of the MRI material. All three segmentation methods performed reasonably well by visual inspection and in most cases they managed to produce an acceptable binary image, regardless of the low image quality and high structural variances in brain. The most robust method was thresholding and all of the 49 images could be segmented using it. In both region growing and k-means clustering nine images had to be excluded due to insufficient segmentation. The images were rejected if either one of structures was missing or if two adjacent structures were connected in the resulting image, even after appropriate parameter adjustments. Most of the problematic images were the same for both methods and the problems could usually be identified with a naked eye.

Even though thresholding is theoretically the simplest method out of the three tested methods, it provided to be the most laborious to perform. The method was troublesome because the threshold level had to be adjusted manually for each image by observing the boundaries of the studied brain structures. This made it very prone to human error. Generally the main problems for the thresholding method are image inhomogeneities and additive noise [36, p. 44]. Intensity inhomogeneities are fundamental to MR scanners [58] and the iron deposition of the brain is asymmetric [59]. These matters make it difficult to determine the threshold level as some areas are more emphasized in the segmentation than the others. Consequently, the brain structures are not segmented equally and at least some of them become distorted. This is probably the main reason why the thresholding segmented images failed to show any differences between the PD patients and controls. Despite the flaws, thresholding has been previously used in medical image analysis in conjunction with other segmentation methods in detecting brain tumors [38][39] and in automatic segmentation of brain tissues [40].

Region growing proved to be significantly faster method for this application than the manual thresholding. It also takes pixel connectivity into account and requires less supervision. Unlike thresholding, region growing is not prone to intensity inhomogeneities as it uses mostly local information [47]. However, there were some differences in the resulting binary images depending on the location of the seed point and, in some cases, the seed points had to be reselected to achieve an acceptable segmentation. This happens because, even after preprocessing, there is still a great variance among the neighbouring pixels in the image. Also the maximum intensity difference of the algorithm had to be adjusted for a few images with low contrast. Region growing also did not show significant differences between patients and controls. The main reason for this is presumably that in many cases the borders of the structures were unclear due to high noise and low contrast. Region growing is not the ideal segmentation method under these conditions because of its pixel-by-pixel approach. In medical imaging, region growing has mostly been used in tumor detection [48][49][50].

K-means clustering proved to be the most promising of the three tested methods as it was the only one that produced statistically significant differences between the two study groups. It required the least amount of operator interaction, as most of the images could be segmented using default settings and the same number of clusters. However, for a couple of images the cluster number had to be increased manually. Although k-means clustering resembles the traditional thresholding methods, it is significantly less prone to uneven pixel intensity distribution of MR images [45]. It is also almost completely unsupervised and does not leave room for human error. K-means clustering is a widely used method for segmentation of brain MR images. For example, it has been used in segmentation of corpus callosum [45] and cerebrospinal fluid, gray matter and white matter [41].

5.2 Shape analysis

Five out of thirteen parameters indicated differences in the left RN between the two study groups in k-means clustering -segmented images. Area, perimeter (Perim.), and Feret's diameter (Feret) are general indicators of the overall size of the structure and their mean values were significantly higher among the patient group. The differences in the height of the bounding rectangle (Height) and the length of the major axis of the best fitting ellipse (Major) and the absence of difference in their counterparts (Width and Minor) indicate that the size of the structure tends to increase in a certain direction. This is also shown by the circularity parameter (Circ.) as the naturally circular red nuclei are less circular in the patient group.

Nine parameters showed differences in the left SNr. As for the lRN, the parameters of overall size (Area, Perim., Height and Feret) were significantly higher among the patient group. The shape of the SNR is naturally more complex than of the circular RN. The complexity is further increased in PD patients, which can be seen by the differences

in the angle of the best fitting ellipse (Angle), circularity (Circ.), the angle of Feret's diameter (FeretAngle) and solidity (Solidity).

The apparent increase of size and irregularity of these structures correlate with the iron accumulation associated with PD [14] and the narrowing of the SNc in MR images [23][24]. The roughness of the outer edge of SNr is also known to increase in PD and it has been detected using T2 weighted 7 T MRI [6]. Similar details cannot be seen in the 3 T images used in this work, but the same phenomenon might have had an effect on the increased irregularity parameters.

5.3 Limitations and sources of error

The main limitation of this work is that only a two dimensional projection of the whole structure was analysed and all of the structural changes related to PD could not be visible. It also makes the normalization of the results problematic. Three dimensional shape analysis and morphometry have provided more comprehensive results from several different brain structures including substantia nigra [6][10][11].

In addition to the segmentation process there are other sources of error regarding the MRI material, the nature of the disease and in the image analysis itself. Even though the study group had been selected carefully, the size of the group was small and most of the patients and controls were female. This is a problem because the prevalence of PD is significantly higher in men and the progression of the disease appears to be slower in women. These differences are thought to be caused by the oestrogen activity and higher striatal dopamine levels of women [60]. However, gender is not known to have effect on natural iron deposition in brain [59]. Another problem is that iron deposition in healthy brain is known to be asymmetric and emphasized in the left hemisphere [59]. This was clearly noticeable in the segmentation process, especially using the thresholding method. It is most likely the main reason why the differences between the patients and the controls could only be observed on the left hemisphere. The right hemisphere could have been analysed more carefully if it was preprocessed and segmented separately.

The imaging was performed using a 3 T MRI device, which is nowadays a standard in clinical neuroimaging. Due to the intrinsic restrictions of MRI the resolution and overall quality of the images is very low compared to the typical applications of the segmentation methods. In this case the image resolution was 288x384 pixels and the areas of the studied structures were between 40 and 220 pixels. This makes even a couple of noisy pixels or the slightest error in segmentation to have a significant impact on the result. Median filter is an effective way to remove single noisy pixels and impulsive noise, but at low resolution and high noise level the filter becomes less efficient. Local variance in intensity values due to magnetic field and RF inhomogeneity is another intrinsic prob-

lem of MR scanners [58]. Global contrast enhancement does not remove this problem entirely and it might have affected the results.

6. CONCLUSIONS

In this Master of Science thesis, quantitative shape analysis was used to study differences in the substantia nigra pars reticulata and in the red nucleus between 29 PD patients and 20 healthy controls. Also the effect of image segmentation method was studied by segmenting the images using three different methods: manual thresholding, seeded region growing and k-means clustering. Thirteen shape factors were calculated for each image and the resulting datasets were analyzed statistically with Mann-Whitney U test to find out whether there were significant differences between the patients and the controls.

Only the k-means clustering segmented images provided statistically significant differences between the patients and the controls and the differences occurred only in the left hemisphere. The results indicate that the sizes of the lRN and the lSNr are greater in the patient group. Circularity values also indicate that the overall shapes of these structures are more irregular in PD patients. These findings correlate with current pathophysiological and anatomical knowledge of PD.

The 2D shape analysis of the RN and the SNr in the left hemisphere showed promising results. Out of the three segmentation methods, the k-means clustering was the one that required the least operator interaction and supervision. It does not require expertise in image processing and it could be easily automatized with the required preprocessing steps. The 13 shape factors calculated in this work were enough to characterize some of the changes related to PD. Some of the shape factors are easy to perceive and they might give exact information of the changes in simple and regular shapes. However, for more complex shapes the information can be misleading and for accurate interpretation several parameters must be studied at once. Further studies, preferably with high-quality 7 T MRI, are needed to evaluate the potential clinical use of this method.

REFERENCES

[1] J. Brown, An Atlas of Parkinson's Disease and Related Disorders, Journal of Neurology, Neurosurgery & Psychiatry, Vol. 66, No. 2, 1999, pp. 257-257.

[2] M. Kasten, A. Chade, C.M. Tanner, Epidemiology of Parkinson's disease, in: Handbook of Clinical Neurology, Elsevier, pp. 129-151.

[3] S. Hung, A. Lang, Differential Diagnosis of Parkinson's Disease, in: CRC Press, 2012, pp. 651-664.

[4] J.T. Bushberg, The Essential Physics of Medical Imaging, Lippincott Williams & Wilkins, 2002, 933 p.

[5] A.G. van der Kolk, J. Hendrikse, J.J.M. Zwanenburg, F. Visser, P.R. Luijten, Clinical applications of 7T MRI in the brain, European Journal of Radiology, Vol. 82, No. 5, pp. 708-718.

[6] D. Kwon, J. Kim, S. Oh, H. Jeong, S. Park, E. Oh, J. Chi, Y. Kim, B.S. Jeon, Z. Cho, Seven-tesla magnetic resonance images of the substantia nigra in Parkinson disease, Annals of Neurology, Vol. 71, No. 2, 2012, pp. 267-277.

[7] S. Lehéricy, E. Bardinet, C. Poupon, M. Vidailhet, C. François, 7 tesla magnetic resonance imaging: A closer look at substantia nigra anatomy in Parkinson's disease, Movement Disorders, Vol. 29, No. 13, 2014, pp. 1574-1581.

[8] L. da Fona Costa, R.M. Cesar, Shape Classification and Analysis: Theory and Practice, Second Edition, CRC Press, 2009, 612 p.

[9] D. Fotiadis, A. Papadopoulos, M. Plissiti, Medical-Image Processing and Analysis for CAD Systems, in: L. Costaridou (ed.), Medical Image Analysis Methods, CRC Press, 2005, pp. 68.

[10] Y. Xiao, P. Jannin, T. D'Albis, N. Guizard, C. Haegelen, F. Lalys, M. Verin, D.L. Collins, Investigation of morphometric variability of subthalamic nucleus, red nucleus, and substantia nigra in advanced Parkinson's disease patients using automatic segmentation and PCA-based analysis, Human brain mapping, Vol. 35, No. 9, 2014, pp. 4330-4344.

[11] F. Nemmi, U. Sabatini, O. Rascol, P. Péran, Parkinson's disease and local atrophy in subcortical nuclei: insight from shape analysis, Neurobiology of aging, Vol. 36, No. 1, pp. 424-433.

[12] N. Sharma, Parkinson's disease, Greenwood Press, Westport, Conn., 2008, .

[13] L. Murrin, Neurochemistry of Parkinson's Disease, in: Neurochemistry of Parkinson's Disease, CRC Press, 2012, pp. 521-528.

[14] J. Wood, MR Imaging of Parkinsonism, in: CRC Press, 2012, pp. 733-748.

[15] E.N. Marieb, K. Hoehn, Human Anatomy & Physiology, 7th ed. Pearson Benjamin Cummings, 2007, 1286 p.

[16] Midbrain, webpage. Available (accessed on 22.9.2015): https://en.wikipedia.org/wiki/Midbrain.

[17] B. Gopalakrishnan, A.J. Stoessl, Dopaminergic Imaging in Parkinson's Disease: PET, in: D. Eidelberg (ed.), Imaging in Parkinson's Disease, Oxford University Press, 2011, pp. 3.

[18] C. Scherfler, W. Poewe, Dopaminergic Imaging in Parkinson's Disease: SPECT, in: D. Eidelberg (ed.), Imaging in Parkinson's Disease, Oxford University Press, 2011, pp. 11.

[19] K. Reetz, F. Binkofski, Structural Abnormalities in Parkinson's Disease: MRI and Related Methods, in: D. Eidelberg (ed.), Imaging in Parkinson's Disease, Oxford University Press, 2011, pp. 32.

[20] J. Hughes, Rehabilitation, occupational therapy and elderly patients with Parkinson's disease, in: Jolyon Meara and William C. Koller. (ed.), Rehabilitation, occupational therapy and elderly patients with Parkinson's disease, Cambridge University Press, Cambridge, 2000, pp. 217-225.

[21] T.A. Zesiewicz, R.A. Hauser, The drug treatment of Parkinson's disease in elderly people, in: Jolyon Meara and William C. Koller. (ed.), The drug treatment of Parkinson's disease in elderly people, Cambridge University Press, Cambridge, 2000, pp. 134-164.

[22] D. Dowsett, P.A. Kenny, R.E. Johnston, The Physics of Diagnostic Imaging, 2nd ed. Taylor & Francis, 2006, 738 p.

[23] J.R. Duguid, R. De La Paz, J. DeGroot, Magnetic resonance imaging of the midbrain in Parkinson's disease, Annals of Neurology, Vol. 20, No. 6, 1986, pp. 744-747.

[24] M.B. Stern, B.H. Braffman, B.E. Skolnick, H.I. Hurtig, R.I. Grossman, Magnetic resonance imaging in Parkinson's disease and parkinsonian syndromes, Neurology, Vol. 39, No. 11, 1989, pp. 1524-1526.

[25] Neuroscience Research Institute Gachon University, Parkinson's and DBS, webpage. Available (accessed on 14.10.2015): http://nri.gachon.ac.kr/b_03_e.html.

[26] M. Hutchinson, U. Raff, Structural Changes of the Substantia Nigra in Parkinson's Disease as Revealed by MR Imaging, American Journal of Neuroradiology, Vol. 21, No. 4, 2000, pp. 697-701.

[27] K. Krabbe, M. Karlsborg, A. Hansen, L. Werdelin, J. Mehlsen, H.B.W. Larsson, O.B. Paulson, Increased intracranial volume in Parkinson's disease, Journal of the neurological sciences, Vol. 239, No. 1, pp. 45-52.

[28] P. Suetens, Fundamentals of Medical Imaging, 2nd ed. Cambridge University Press, Cambridge, 2009, 264 p.

[29] K. Yoshikawa, Y. Nakata, K. Yamada, M. Nakagawa, Early pathological changes in the parkinsonian brain demonstrated by diffusion tensor MRI, Journal of Neurology, Neurosurgery & Psychiatry, Vol. 75, No. 3, 2004, pp. 481-484.

[30] L. Chan, H. Rumpel, K. Yap, E. Lee, H. Loo, G. Ho, S. Fook-Chong, Y. Yuen, E. Tan, Case control study of diffusion tensor imaging in Parkinson's disease, Journal of Neurology, Neurosurgery & Psychiatry, Vol. 78, No. 12, 2007, pp. 1383-1386.

[31] D.E. Vaillancourt, M.B. Spraker, J. Prodoehl, I. Abraham, D.M. Corcos, X.J. Zhou, C.L. Comella, D.M. Little, High-resolution diffusion tensor imaging in the substantia nigra of de novo Parkinson disease, Neurology, Vol. 72, No. 16, 2009, pp. 1378-1384.

[32] I.L. Dryden, K.V. Mardia, Statistical Shape Analysis, Wiley, 1998, 376 p.

[33] L. Hopes, G. Grolez, C. Moreau, R. Lopes, G. Ryckewaert, N. Carrière, F. Auger, C. Laloux, M. Petrault, J. Devedjian, R. Bordet, L. Defebvre, P. Jissendi, C. Delmaire, D. Devos, Magnetic Resonance Imaging Features of the Nigrostriatal System: Biomarkers of Parkinson's Disease Stages, PLoS ONE, Vol. 11, No. 4, 2016, pp. e0147947.

[34] J.C. Russ, The Image Processing Handbook, Sixth Edition, 6th ed. CRC Press, Inc, Boca Raton, FL, USA, 2011, 885 p.

[35] R.C. Gonzalez, R.E. Woods, Digital Image Processing, 2nd ed. Addison-Wesley Longman Publishing Co., Inc, Boston, MA, USA, 2001, 812 p.

[36] M. Haidekker, Advanced Biomedical Image Analysis, Wiley, 2011, 541 p.

[37] A.K. Jain, R.C. Dubes, Algorithms for Clustering Data, Prentice-Hall, Inc, Upper Saddle River, NJ, USA, 1988, 334 p.

[38] H.S. Abdulbaqi, M.Z. Mat, A.F. Omar, I.S. Bin Mustafa, L.K. Abood, Detecting brain tumor in Magnetic Resonance Images using Hidden Markov Random Fields and Threshold techniques, Research and Development (SCOReD), 2014 IEEE Student Conference on, pp. 1-5.

[39] P. Natarajan, N. Krishnan, N.S. Kenkre, S. Nancy, B.P. Singh, Tumor detection using threshold operation in MRI brain images, Computational Intelligence & Computing Research (ICCIC), 2012 IEEE International Conference on, pp. 1-4.

[40] K.J. Shanthi, M.S. Kumar, Skull stripping and automatic segmentation of brain MRI using seed growth and threshold techniques, Intelligent and Advanced Systems, 2007. ICIAS 2007. International Conference on, pp. 422-426.

[41] S.S.K. Nair, K. Revathy, Quantitative Analysis of Brain Tissues from Magnetic Resonance Images, Digital Image Processing, 2009 International Conference on, pp. 57-61.

[42] J. Han, M. Kamber, J. Pei, 10 - Cluster Analysis: Basic Concepts and Methods, in: J.H. Kamber, J. Pei (ed.), Data Mining (Third Edition), Morgan Kaufmann, Boston, 2012, pp. 443-495.

[43] D.T. Pham, S.S. Dimov, C.D. Nguyen, Selection of K in K-means clustering, Proceedings of the Institution of Mechanical Engineers, Part C: Journal of Mechanical Engineering Science, Vol. 219, No. 1, 2005, pp. 103-119.

[44] D. Arthur, S. Vassilvitskii, K-means++: The Advantages of Careful Seeding, Proceedings of the Eighteenth Annual ACM-SIAM Symposium on Discrete Algorithms, Society for Industrial and Applied Mathematics, Philadelphia, PA, USA, pp. 1027-1035.

[45] G.V. Bhalerao, N. Sampathila, K-means clustering approach for segmentation of corpus callosum from brain magnetic resonance images, Circuits, Communication, Control and Computing (I4C), 2014 International Conference on, pp. 434-437.

[46] R.M. Rangayyan, Biomedical Image Analysis, CRC Press, 2004, 1311 p.

[47] R. Adams, L. Bischof, Seeded region growing, Pattern Analysis and Machine Intelligence, IEEE Transactions on, Vol. 16, No. 6, 1994, pp. 641-647.

[48] L. Ramya, N. Sasirekha, A robust segmentation algorithm using morphological operators for detection of tumor in MRI, Innovations in Information, Embedded and Communication Systems (ICIIECS), 2015 International Conference on, pp. 1-4.

[49] A.R. Kavitha, C. Chellamuthu, K. Rupa, An efficient approach for brain tumour detection based on modified region growing and neural network in MRI images, Computing, Electronics and Electrical Technologies (ICCEET), 2012 International Conference on, pp. 1087-1095.

[50] T. Weglinski, A. Fabijanska, Brain tumor segmentation from MRI data sets using region growing approach, Perspective Technologies and Methods in MEMS Design (MEMSTECH), 2011 Proceedings of VIIth International Conference on, pp. 185-188.

[51] D.R. Caldwell, Unlocking the Mysteries of the Bounding Box, webpage. Available (accessed on 13.11.2015): http://purl.oclc.org/coordinates/a2.htm.

[52] M. Stojmenovic, A. Nayak, Direct Ellipse Fitting and Measuring Based on Shape Boundaries, in: D. Mery, L. Rueda (ed.), Springer Berlin Heidelberg, 2007, pp. 221-235.

[53] ImageJ, Image Processing and Analysis in Java, webpage. Available (accessed on 22.9.2015): http://imagej.nih.gov/ij/.

[54] ImageJ Documentation: Filters, webpage. Available (accessed on 22.9.2015): http://rsb.info.nih.gov/ij/docs/menus/process.html#filters.

[55] IJ Plugins, custom plugins for the ImageJ software package, webpage. Available (accessed on 22.9.2015): http://ij-plugins.sourceforge.net/.

[56] Matlab Central File Exchange: Fast 3D/2D Region Growing (MEX), webpage. Available (accessed on 22.9.2015): http://in.mathworks.com/matlabcentral/fileexchange/41666-fast-3d-2d-region-growing--mex-.

[57] ImageJ Documentation: Set Measurements, webpage. Available (accessed on 18.3.2015): http://rsb.info.nih.gov/ij/docs/menus/analyze.html#set.

[58] D. Selvaraj, R. Dhanasekaran, Novel approach for segmentation of brain magnetic resonance imaging using intensity based thresholding, Communication Control and Computing Technologies (ICCCCT), 2010 IEEE International Conference on, pp. 502-507.

[59] X. Xu, Q. Wang, M. Zhang, Age, gender, and hemispheric differences in iron deposition in the human brain: An in vivo MRI study, NeuroImage, Vol. 40, No. 1, 2008, pp. 35-42.

[60] C.A. Haaxma, B.R. Bloem, G.F. Borm, W.J.G. Oyen, K.L. Leenders, S. Eshuis, J. Booij, D.E. Dluzen, M.W.I.M. Horstink, Gender differences in Parkinson's disease, Journal of neurology, neurosurgery, and psychiatry, Vol. 78, No. 8, 2006, pp. 819-824.

APPENDIX 1: IMAGEJ SHAPE PARAMETERS

Parameter	Description
Area	Area of selection in selected units
Perim.	Perimeter, the length of the boundary
BX	X-coordinate of the upper left corner of the bounding rectangle
BY	Y-coordinate of the upper left corner of the bounding rectangle
Width	Width of the bounding rectangle
Height	Height of the bounding rectangle
Major	Primary axis of the best fitting ellipse
Minor	Secondary axis the best fitting ellipse
Angle	Angle between the primary axis of the best fitting ellipse and a line parallel to the X-axis of the image
Circ.	Circularity. See equation 11.
Feret	Feret's diameter. The maximum diameter of the object
FeretX	X-coordinate of the starting point of Feret's diameter
FeretY	Y-coordinate of the starting point of Feret's diameter
FeretAngle	The angle of Feret's diameter
MinFeret	The minimum diameter of the object
AR	Aspect ratio
Round	Inverse of aspect ratio
Solidity	Solidity, see equation 13

APPENDIX 2: SHAPE ANALYSIS RESULTS

		P values, control vs. patient (statistically significant (p < 0.005) values are bolded)												
Segmentation	**Structure**	**Area**	**Perim.**	**Width**	**Height**	**Major**	**Minor**	**Angle**	**Circ.**	**Feret**	**FeretAngle**	**MinFeret**	**AR**	**Solidity**
Thresholding	Left RN	0.496	0.661	0.214	0.226	0.579	0.817	0.679	0.562	0.502	0.721	1.000	0.377	0.440
	Right RN	0.513	0.436	0.970	0.247	0.559	0.627	0.520	0.382	0.987	0.871	0.484	0.711	0.394
	Left SNr	0.416	0.219	0.582	0.307	0.253	0.782	0.136	0.154	0.207	0.092	0.836	0.229	0.361
	Right SNr	0.200	0.315	0.703	0.493	0.369	0.474	0.461	0.743	0.350	0.259	0.661	0.694	0.713
Region growing	Left RN	0.670	0.642	0.580	0.300	0.483	0.623	0.799	0.355	0.614	0.443	0.612	**0.041**	0.799
	Right RN	0.451	0.434	0.611	0.654	0.757	0.619	0.654	0.494	0.804	0.788	0.520	0.684	0.486
	Left SNr	0.623	0.525	0.837	0.389	0.284	0.860	0.500	0.362	0.261	0.901	0.642	0.661	0.138
	Right SNr	0.566	0.410	0.412	0.564	0.406	0.961	0.439	0.494	0.357	0.062	0.852	0.255	0.585
K-means clustering	Left RN	**0.048**	**0.042**	0.447	**0.016**	**0.034**	0.359	0.594	**0.047**	**0.026**	0.769	0.324	0.112	0.801
	Right RN	0.334	0.230	0.283	0.264	0.149	0.486	0.946	**0.042**	0.213	0.918	0.487	0.482	0.832
	Left SNr	**0.029**	**0.007**	0.198	**0.039**	0.051	0.101	**0.012**	**0.012**	**0.024**	**0.015**	**0.014**	0.486	**0.047**
	Right SNr	0.875	0.918	1.000	0.918	0.881	0.817	0.539	0.590	0.918	0.424	0.886	0.613	0.416